Pattern scaling of simulated vegetation change in North Africa during glacial cycles

Mateo Duque-Villegas[1,2], Martin Claussen[1,3], Thomas Kleinen[1], Jürgen Bader[4], and Christian H. Reick[1]

[1]Max Planck Institute for Meteorology, Hamburg, Germany
[2]International Max Planck Research School on Earth System Modelling, Hamburg, Germany
[3]Meteorological Institute, Center for Earth System Research and Sustainability (CEN), Universität Hamburg, Hamburg, Germany
[4]Institute of Oceanography, Center for Earth System Research and Sustainability (CEN), Universität Hamburg, Hamburg, Germany

Correspondence: Mateo Duque-Villegas (mateo.duque@mpimet.mpg.de)

Abstract. Over the last hundreds of millennia, natural rhythms in Earth's astronomical motions triggered large-scale climate changes and led periodically to humid conditions in much of North Africa. Known as African Humid Periods (AHPs), such times sustained vast river networks, vegetation, wildlife, and prehistoric settlements. Mechanisms, extent, and timing of the changes remain poorly constrained. Although AHPs along glacial cycles are recognizable in marine sediment records, the related land cover changes are difficult to reconstruct due to scarcity of proxy data over the continent. Moreover, most available information covers only the latest AHP during the Holocene. Here we use a comprehensive Earth system model to look at additional, much earlier, possible cases of AHPs. We simulate the full last glacial cycle, aiming to reproduce the last four AHPs as seen in available proxies. The simulated AHPs seem in broad agreement with geological records, especially in terms of timing and relative strength. We focus on the simulated vegetation coverage in North Africa, and we detect a dominant change pattern that seems to scale linearly with known climate forcing variables. We use such scaling to approximate North African vegetation fractions over the last eight glacial cycles. Although the simple linear estimation is based on a single mode of vegetation variability (that explains about 70% of the variance), it helps to discuss some broad-scale spatial features that had been only considered for the Holocene AHP. Extending the climate simulation several millennia into the future reveals that such (palaeo-based) pattern scaling breaks when greenhouse gases become a stronger climate change driver.

1 Introduction

Broad swings in environmental conditions over North Africa have happened for at least the last 11 million years (Crocker et al., 2022). What is today the hyper-arid Sahara was formerly at times a much wetter region, adequate for sustaining perennial water bodies and vast expanses of vegetation cover that significantly reduced dust output to surrounding areas (Gasse, 2000; deMenocal et al., 2000). Such times, known also as African Humid Periods (AHPs), were recorded as quasi-periodic intervals of enhanced moist conditions in regional geological archives (Grant et al., 2017, 2022). Humid climates set in along with changes in the land surface that via feedback loops amplified the effects of changes in the Earth's orbit on the distribution of

incoming solar radiation (Claussen et al., 2017; Pausata et al., 2020). Extent and timing of the changes remain uncertain due to proxy data limitations (Yacoub et al., 2023), while understanding of the causes and mechanisms is incomplete as evinced in persistent discrepancies between existing geological records and climate simulations (Brierley et al., 2020).

25   The Holocene interglacial had the best known case of an AHP, spanning roughly between $11.7\,ka$ to $4.2\,ka$ (ka is thousands of years ago) (Claussen et al., 2017). Evidence collected for this period around North Africa revealed the changes in past lake highstands (Lézine et al., 2011), river networks (Drake et al., 2011), dust fluxes (McGee et al., 2013), vegetation cover (Hély et al., 2014) and rainfall (Tierney et al., 2017b). In addition, numerical climate models were able to reproduce some of these changes during the Holocene AHP, and hinted at basic mechanisms underpinning AHP dynamics (Claussen et al., 2017). Proxy

30 data and models spurred an interesting debate that highlighted the spatial and temporal complexities of an AHP, since spatial heterogeneity resulted in marked differences in localized rates of change and asynchronous AHP termination across North Africa (Brovkin and Claussen, 2008; Shanahan et al., 2015; Dallmeyer et al., 2020). Nevertheless, what happened before the Holocene and how known mechanisms played a role in even deeper times is relatively unknown. Repeated climate and land cover changes prevented preservation of geological records older than the Holocene over land (Drake et al., 2018), while the

35 costs of complexity and spatial and temporal resolutions limited in many cases the reach of simulations with comprehensive climate models (Tierney et al., 2020a).

    What is known about pre-Holocene AHPs is mainly informed by signals recorded in marine sediments off the North African coastline. Marine proxies, combined with the few surviving terrestrial signatures, and taking the Holocene AHP as a baseline, make it possible to examine the cases of AHPs along glacial cycles (Blome et al., 2012; Drake et al., 2013; Larrasoaña et al.,

40 2013; Scerri et al., 2014). For instance, the multiple lines of geological evidence suggest that the previous interglacial during Marine Isotope Stage (MIS) 5e, near $127\,ka$, most likely had a much stronger AHP than the Holocene, in agreement with modelling results about the influence of changes in Earth's orbit. Likewise, marine proxies from around North Africa show other potential AHPs during the last few glacial cycles (e.g. Rossignol-Strick, 1983; Ehrmann and Schmiedl, 2021). However, limitations in projecting marine proxy signals far inland, compounded with scant terrestrial sources, restrict our understanding

45 about the amplitude of North African climate variability and AHP development. A clear outline of AHP changes is crucial to explain, for instance, regional geomorphology (Drake et al., 2022), ecological corridors during hominin evolution (Scerri et al., 2018) and long-term climate–land surface interactions (Pausata et al., 2020).

    Climate models offer a theoretical window into possible spatial patterns of AHPs. For instance, early experiments with an atmosphere-only model already coarsely simulated four AHPs since $150\,ka$ (Prell and Kutzbach, 1987), as many as indicated

50 by marine proxies. However, modelling long glacial cycles to include multiple AHPs requires a compromise between model complexity, simulation length and spatial resolution, which hinders the amount of detail that can be reproduced and evaluated. Studies that kept relatively complex models and higher spatial resolutions chose to either simulate discontinuous time slices (Singarayer and Burrough, 2015), or accelerate climate forcing rates (Kutzbach et al., 2008, 2020); in both cases reducing the effects of high-frequency variability. Other studies opted for intermediate complexity models and large grid spacings to focus

55 mostly on temporal patterns of average changes of AHPs (e.g. Tuenter et al., 2003; Tjallingii et al., 2008; Menviel et al., 2021).

Although simulations broadly agreed with trends in the proxy records, underestimation of Saharan shrinking during AHPs and associated rainfall increments is a consistent problem across models, questioning current understanding on the mechanisms and scale of the changes. Simulating a full glacial cycle with interactive climate and vegetation components at higher spatial resolution may reveal dominant AHP patterns underlying geological records or behind data–model mismatches.

We use the comprehensive Max Planck Institute for Meteorology Earth System Model (MPI-ESM; Giorgetta et al., 2013) to perform a transient global climate simulation since 134 ka, at an affordable spatial resolution to see subcontinental changes in vegetation cover of North Africa. The main goal is to find general trends in simulated patterns during AHPs of the last glacial cycle. We evaluate the vegetation cover of different AHP responses and relate it explicitly with the large-scale climate drivers: (1) Earth's orbital parameters, (2) radiative effects of levels of atmospheric greenhouse gases (GHG) and (3) high-latitude ice sheets. These drivers are known to set multiple controls on localized rain-bringing mechanisms (Dallmeyer et al., 2020; Blanchet et al., 2021), which could lead to diverse AHP biogeographies. Assuming local environments reacted always similarly to climate forcing, it is possible that AHP vegetation patterns be approximated as a function of known forcing values. In addition, we also simulate and briefly assess potential future evolution of North African vegetation. In the following sections we describe the climate model, explain the experimental set-up, present results focused on North African vegetation cover during AHPs and discuss the possibility of a forcing-based pattern scaling.

2   Methods

2.1   Model description

We use version 1.2 of MPI-ESM (Mauritsen et al., 2019). The model couples dynamical components representing the general circulations of the atmosphere (ECHAM6.3; Stevens et al., 2013) and ocean (MPIOM1.6; Jungclaus et al., 2013), as well as changes in the land surface and vegetation cover (JSBACH3.2; Reick et al., 2013). The standard release of this model version participated in the Coupled Model Inter-comparison Project Phase Six (CMIP6; Eyring et al., 2016). Implementation of the coarse resolution set-up T31GR30 (about $3.75°$ horizontally) with 31 atmospheric and 40 oceanic levels enables long climate simulations at about maximum 700 simulated years per day (Mikolajewicz et al., 2018). Simulations covering several glacial cycles require updates during runtime of the land-sea mask, glacier mask and river routing, that align with reconstructions of ice-sheet and sea-level changes. This is done once every decade as described in Meccia and Mikolajewicz (2018) and Riddick et al. (2018). The specific model set-up is actively maintained and performs well within the range of current general circulation models (Kapsch et al., 2022).

How the model computes natural vegetation cover is particularly relevant for this study. A detailed description is given in Reick et al. (2013) and a performance assessment is in Brovkin et al. (2013). Briefly, the model uses a "mosaic" approach where each land surface grid cell is tiled to be occupied by fractions of predefined plant functional types (PFTs). PFTs include eight cover classes between woody (tropical and extra-tropical trees plus shrubs) and herbaceous (C3 and C4 grasses) vegetation, each with different turn-over timescales. When one vegetation type dies via natural causes (age) or via disturbances (fire or

wind-throw), the "void" it leaves is filled (or "colonized") by growth of the most competitive PFT in terms of net primary productivity (NPP), which is a function of climate and atmospheric CO_2. Seeds for all PFTs are assumed to be universally present. Fractions of PFTs can only occupy the portion of a grid cell that is hospitable for growth, which is determined based on having sufficiently productive (NPP) vegetation over consecutive years. The distribution of inhospitable fractions across the globe corresponds to hot and cold deserts. Vegetation cover in the model has immediate effects on the exchange processes between land surface and the atmosphere, which can subsequently alter climate patterns and feedback on vegetation (Brovkin et al., 2009).

2.2 Experiments

We simulate a transient Earth-system response to prescribed forcing for the last $134\,\mathrm{kyr}$ (kyr is thousand years as in duration), almost entirely as a single continuous run ($120\,\mathrm{ka}$ to $0\,\mathrm{ka}$), except for a 14-kyr interval spliced a posteriori to extend analysis until $134\,\mathrm{ka}$ (details about splicing in Appendix A). Earth's orbital parameters are computed from Berger (1978). Atmospheric levels of GHG (CO_2, CH_4 and N_2O) are taken from the ice core records compilation of Köhler et al. (2017), and are updated every 10 model years as decadal means. Ice sheets from the GLAC-1D dataset (Tarasov and Peltier, 2002; Tarasov et al., 2012, 2014; Briggs et al., 2014; Abe-Ouchi et al., 2013) are interpolated spatially and temporally to suit model resolution and are prescribed also at decennial time steps, with corresponding adjustments in topography, bathymetry and river routing (Meccia and Mikolajewicz, 2018; Riddick et al., 2018). Details about the GLAC-1D dataset extension until before the last interglacial are given in Menviel et al. (2019).

Figure 1 (left) compiles a set of variables directly linked to forcing factors: orbitally driven changes in low-latitude insolation in terms of the so-called orbital monsoon index (Fig. 1a); the Northern Hemisphere total volume of ice sheets (Fig. 1b); and the GHG radiative forcing change relative to the pre-industrial era (PI, 1850 Common Era or CE; Fig. 1c). The monsoon index of Rossignol-Strick (1983) is an insolation difference between the Northern Tropic ($23.4°\,\mathrm{N}$) and the equator during the caloric summer season defined by Milankovitch (1941). Changes in the radiative forcing of GHG are based on an "equivalent-CO_2 concentration" explained in Ganopolski et al. (2010). We ignore any land use and atmospheric aerosols remain at pre-industrial values (Kinne et al., 2013). Figure 1 includes also MIS labels according to Railsback et al. (2015), which we use throughout the text simply to refer to approximate ages of the late Quaternary when an AHP may have occurred.

Additionally, we run two transient experiments $10\,\mathrm{kyr}$ into the future. In both, the ice sheets remain unchanged at present-day conditions, while the orbital forcing continues to change according to Berger (1978). Such an approximation for the ice sheets is based on the study of Ganopolski et al. (2016), where they suggest no substantial changes are expected within the next several millennia. For GHG concentrations we choose two alternative Shared Socioeconomic Pathway (SSP) scenarios from the Sixth Assessment Report (AR6) of the Intergovernmental Panel on Climate Change (IPCC): SSP1-1.9 and SSP3-7.0 (IPCC, 2021). The two scenarios are selected simply as contrasting cases of potential future GHG dominance. The GHG data for these scenarios come from Meinshausen et al. (2020) until the year $2500\,\mathrm{CE}$, and onwards from previous modelling output of Brovkin et al. (2012), similarly as in Kleinen et al. (2021).
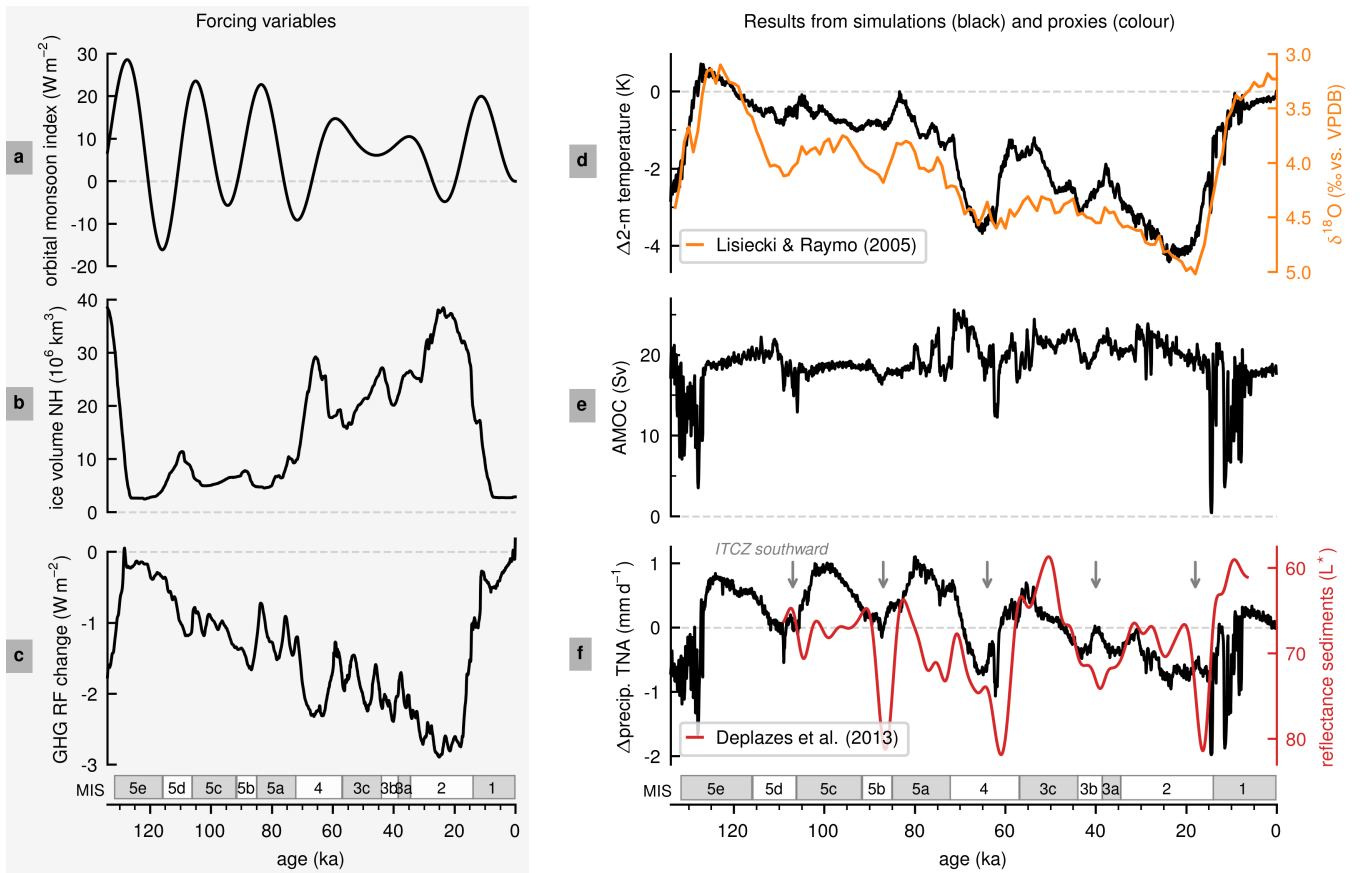
Figure 1. Transient simulation of the last glacial cycle. Forcing variables (left) represent prescribed conditions driving the experiment: (a) orbital parameters following Berger (1978) are shown using the orbital monsoon index of Rossignol-Strick (1983); (b) ice sheets from the GLAC-1D dataset (references in main text) are shown with the total ice volume in the Northern Hemisphere (NH); and (c) greenhouse gases (GHG) from Köhler et al. (2017) are shown as radiative forcing (RF) changes from pre-industrial era (PI). Simulation results compared with proxy records (right): (d) changes in global mean near-surface temperature relative to PI, compared to isotopic data from Lisiecki and Raymo (2005); (e) Atlantic meridional overturning circulation (AMOC) in the Atlantic Ocean (1000-m depth, basin mean at $26° N$); and (f) changes in precipitation in the Tropical North Atlantic (TNA; defined in main text) compared to marine sediments reflectance ($L^\star$; smoothed with a third-order low-pass Butterworth filter with a cutoff frequency of $1/5\,\mathrm{kyr}^{-1}$) data from Deplazes et al. (2013), both related to shifts of the Inter-Tropical Convergence Zone (ITCZ). We include labels for marine isotope stages (MIS) according to Railsback et al. (2015).

3   Results

We average the simulation results as annual means at centennial scale. In the following sections we present our results first from a simulated global context and then we focus on the past and future of AHPs. We analyze the simulated AHPs of the last glacial cycle and develop a pattern scaling approach that is useful to also explore much older AHPs of the late Quaternary.

125 Then we look at simulated future AHPs and how they compare to the pattern scaling method. Whenever possible we compare model output to proxy results and insights from previous modelling experiences.

3.1 Earth-system response

Figure 1 (right) shows some globally relevant mean climate variables. Global climate is the warmest during the MIS 5e interglacial near $127\,\text{ka}$ (Fig. 1d). About $0.7\,\text{K}$ warmer than simulated pre-industrial temperature, the last interglacial warming

130 matches proxies in the sign of change, but the amount could be underestimated by up to $1.3\,\text{K}$ (Turney et al., 2020), similarly as in other climate models (Lunt et al., 2013; Otto-Bliesner et al., 2021). Minimum average temperature occurs during the Last Glacial Maximum (LGM) around $24\,\text{ka}$, with roughly $4.4\,\text{K}$ colder than during PI, which is not far from recent estimates ranging from $5\,\text{K}$ to $7\,\text{K}$ (Tierney et al., 2020b; Osman et al., 2021). Amplitude and timing of temperature changes seem in agreement with the isotopic data from Lisiecki and Raymo (2005).

135 Ocean dynamics maintains an Atlantic meridional overturning circulation (AMOC) around $19\,\text{Sv}$ (Fig. 1e), including millennial-scale fluctuations related to freshwater input from glacier run-off as the ice sheets change. Strongest AMOC variability occurs during late deglaciation phases around $130\,\text{ka}$ to $128\,\text{ka}$ and $15\,\text{ka}$ to $9\,\text{ka}$. The last deglaciation includes an especially strong meltwater pulse near $14.4\,\text{ka}$ that nearly collapses the AMOC in the simulation (Kleinen et al., 2023). After this meltwater pulse, the remainder of the simulation includes some unexpected AMOC variability during the early Holocene. The

140 amplitude of this early-Holocene AMOC variability is not represented in the meltwater release from the ice-sheet reconstruction, and it was not seen in previous deglaciation experiments with the same model (e.g. Kapsch et al., 2022; Kleinen et al., 2023). In our simulation it appears to be related to a slight difference in the initial condition of ocean volume that results in some shallow regions in the Arctic Ocean. The AMOC changes are associated with drops in global temperature and in precipitation in the tropics (see Fig. 1d and f).

145 As a proxy for large-scale circulation changes in the atmosphere, we also show in Fig. 1f the simulated precipitation changes in the Tropical North Atlantic (TNA; $10°\,\text{N}$ to $20°\,\text{N}$, $80°\,\text{W}$ to $20°\,\text{W}$), where changes are coupled to movements in the average position of the Inter-Tropical Convergence Zone (ITCZ). Unlike global temperature, these changes follow more closely the oscillations of the orbital monsoon index, and the timing of the minima of precipitation (when the ITCZ is southernmost) broadly agrees with the Cariaco Basin record of Deplazes et al. (2013). The Cariaco Basin record shows total reflectance

150 values of dark/light segments in a sediment core extracted off the coast of Venezuela, which relate to rather enhanced (low L^*) or rather suppressed (high L^*) rainfall rates and hence tracked displacements of the ITCZ (Deplazes et al., 2013). However, the simulation is slightly out of phase with the proxy record and not all excursions from mean values are matching, probably because of regional or local scale signals in the data and the issues of smoothing both time series.
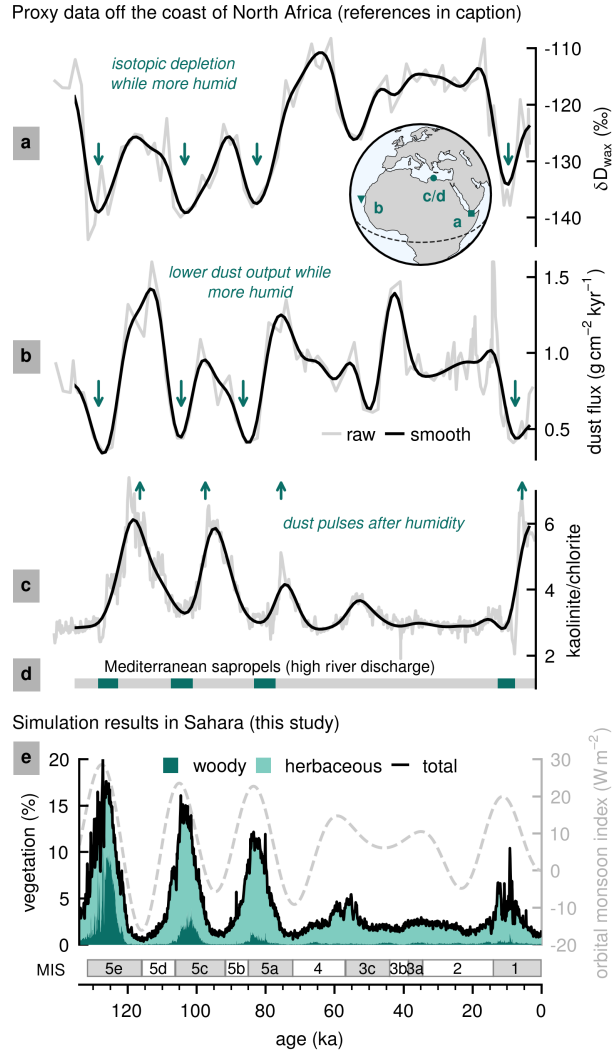
Figure 2. North African climate in the last glacial cycle as seen in (a–d) marine proxies offshore and (e) average simulated vegetation coverage (woody, herbaceous and total) in the Sahara (defined in main text). Proxy data (grey) are interpolated evenly at $1\,\mathrm{kyr}$ resolution and smoothed (black) with a third-order low-pass Butterworth filter with a cutoff frequency of $1/10\,\mathrm{kyr}^{-1}$: (a) deuterium ratio changes (δD) in terrestrial plant lipids (wax) in core RC09-166 near eastern Africa (Tierney et al., 2017a); (b) ^{230}Th-normalized Saharan dust flux into the Atlantic Ocean according to core MD03-2705 near West Africa (Skonieczny et al., 2019); (c) influx of fine-sized dust to the Eastern Mediterranean Sea according to the ratio of kaolinite and chlorite minerals in core SL99 and (d) its sapropel sequence (Ehrmann and Schmiedl, 2021). In (e) we also show a secondary y-axis with the orbital monsoon index. Proxy sites are shown in an inset globe.

3.2 African Humid Periods

3.2.1 Timing and strength

Marine sediments off the coast of North Africa reveal four AHPs in the last $134\,\mathrm{kyr}$ (Fig. 2a–d). AHPs appear as times of pronounced depletion of deuterium (D) ratios in leaf waxes from around eastern Africa (Tierney et al., 2017a) as a result of increased rainfall (Fig. 2a). AHPs can also be seen as times of reduced Saharan dust output to the Atlantic Ocean (Skonieczny et al., 2019) and Mediterranean Sea (Ehrmann and Schmiedl, 2021), because increased soil-stabilising vegetation cover restricted dust deflation (Fig. 2b, c). Likewise, during AHPs increased river discharge into the Mediterranean stratified seawater and promoted the formation of sapropel bands (Fig. 2d). In spite of notable differences in location and methods amongst proxy records, AHPs stand out rather consistently.

Focusing on the kaolinite/chlorite proxy (Fig. 2c), it reveals details about the intensity of the AHPs, according to the amplitude of dust pulses, which depends on the degree of (rain-fed) weathering that accumulates the kaolinite mineral in water bodies while an AHP is active (Ehrmann et al., 2017). Accordingly, in Fig. 2c, the AHP of MIS 5e stands out clearly as the strongest (largest dust pulse near $118\,\mathrm{ka}$), while the estimated magnitude of other AHPs based on kaolinite/chlorite has been indicated to vary with the core-to-shore distance (Ehrmann and Schmiedl, 2021).

Figure 2e shows simulation results of total vegetation fraction in the Sahara ($20°\,\mathrm{N}$ to $30°\,\mathrm{N}$, $20°\,\mathrm{W}$ to $25°\,\mathrm{E}$). The simulation appears well in phase with trends in the geological records. We find four AHP-like changes in North African climate, seen as large peaks in average Saharan vegetation. The vegetation peaks track the orbital monsoon index but with a small lag of about $1\,\mathrm{kyr}$, which is longer than required for the vegetation to expand over the region. Most of this lag probably appears because the orbital monsoon index is tied to the summer season only and to the Northern Tropic ($23.4°\,\mathrm{N}$), while the simulated vegetation response is also affected by what happens in the extra-tropics, not only in the summer but also during the winter season. Saharan vegetation peaks happen sometime between peak boreal summer temperatures and mild boreal winter temperatures.

Simulated AHPs appear also as times of herbaceous cover expansion and woody types invasion of the Sahara. The AHP of MIS 5e is the strongest event with above $15\,\%$ Saharan vegetation cover, followed by two weaker AHPs during MIS 5c and 5a (near $103\,\mathrm{ka}$ and $83\,\mathrm{ka}$, respectively), both clearly over $10\,\%$ total vegetation fraction. In the simulation the Holocene has the weakest AHP, barely approaching $10\,\%$ of vegetation in the Sahara. Such a weak Holocene AHP is unexpected according to previous applications of the same model to the last deglaciation (e.g. Dallmeyer et al., 2022).

In our simulation the Holocene climate is unexpectedly largely affected by pronounced AMOC variability (cf. Fig. 1e), whose amplitude is greater than prescribed with the ice-sheet reconstruction changes (unlike MIS 5e where AMOC fluctuations are according to ice-sheet changes). The large AMOC fluctuations appear connected with a small ocean volume difference in the initial condition of the experiment. To diagnose the weak Holocene AHP we include Appendix B, where we show the global climate anomalies with respect to pre-industrial temperature and precipitation. The effects of the AMOC variability are clearly seen in the early Holocene having a much colder North Atlantic region (Fig. B1f). This keeps the ITCZ and related rain bands southward and explains the anomalously weak Holocene AHP (see Tjallingii et al., 2008).
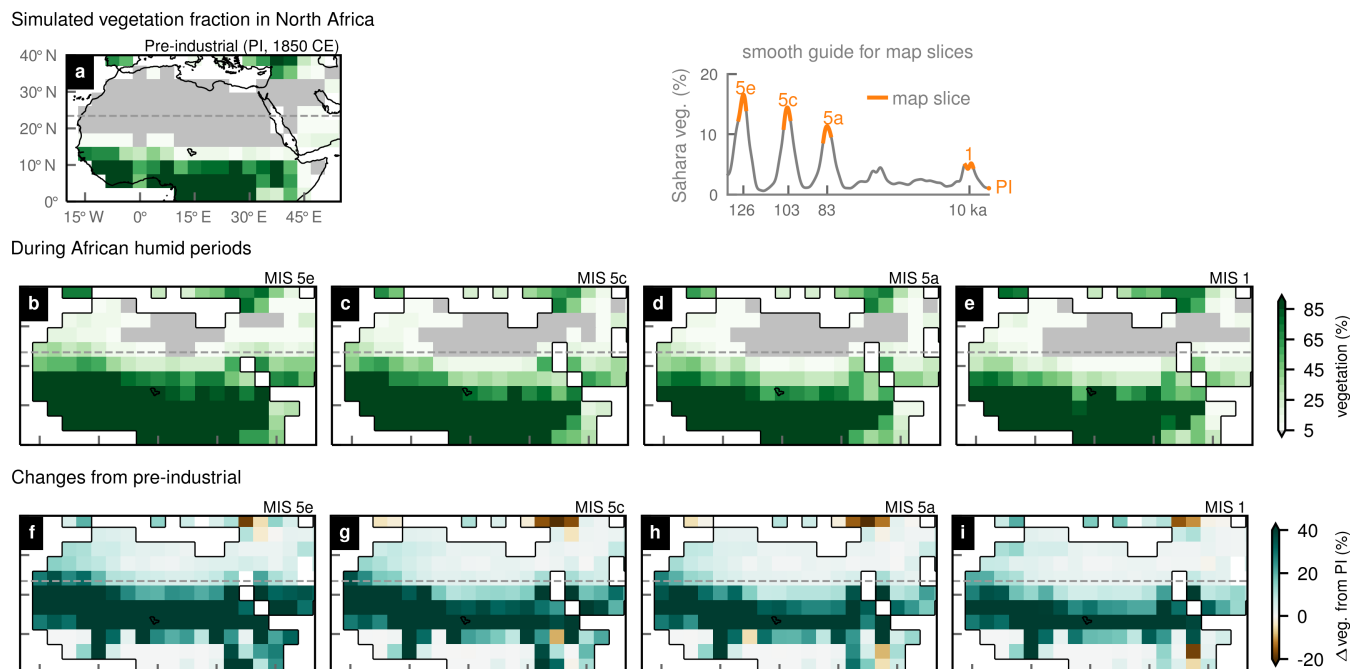
Figure 3. North African vegetation coverage. (a–e) Maximum vegetation coverage during pre-industrial (PI) era and AHPs, as well as (f–i) the relative changes from PI. A time series inset (top right) has marine isotope stages (MIS) labels to highlight mapped AHP time slices spanning about $4\,\mathrm{kyr}$. In maps a horizontal line shows the Northern Tropic ($23.4°\,\mathrm{N}$). Only the PI map shows modern coastlines, while others show the coastlines according to reconstructed sea-level changes. Lake Chad is shown in all maps as a point of reference.

Nevertheless, strength of AHPs in Fig. 2e is meant only relative to each other, since an overall Sahara greening below $20\,\%$ is still substantially less than previous estimates from intermediate complexity models (e.g. Menviel et al., 2021; Duque-Villegas et al., 2022), as well as less than estimates from the same model but implemented at higher spatial resolution (Dallmeyer et al., 2020). In Appendix C there is a brief comparison of the simulated climate near present-day (mean values for 1990–2020 CE) with current observational products. We find the model simulates less vegetation in the Sahel (despite neglecting land use in the simulation), and overall is much drier (about $1\,\mathrm{mm\,d^{-1}}$) over North Africa than inferred from the observational data. Explaining the mismatch between different complexity models or why there is a dry bias in the model at this spatial resolution is beyond the scope of this work, thus we focus on relative changes rather than absolute values.

3.2.2 Vegetation patterns

The intensity of an AHP should manifest also in the spatial extent of changes in vegetation coverage. Figure 3 shows maximum vegetation cover fraction in North Africa during AHPs and changes from PI. In this case AHP values are selected from time slices around the vegetation optimum in the Sahara (see guide in figure). It is important to note that it is not trivial to define AHPs for the whole North Africa, since it is a large region that responds with spatio-temporal heterogeneity (see Dallmeyer

200   et al., 2020). For this reason we show maximum values that may happen at different times (a few centuries earlier or later) for different sites (grid points) within an AHP time slice. Spatial heterogeneity leads to an interesting distinction about the changes in Fig. 3, between areas that are already "green" for pre-industrial conditions (like below the Sahel), which become "greener" during AHPs, and areas that are barren at PI which *turn* "green" during AHPs (like inside the Sahara).

Pre-industrial conditions in the simulation (Fig. 3a) already seem to underestimate zonal patterns of vegetation (like present-
205   day dry bias in Appendix C), resulting in little vegetation in the Sahel (near $15°$ N) and an exaggerated Dahomey Gap (dividing the Coast of Guinea) that is much less conspicuous in higher resolution versions of the same climate model (e.g. Bathiany et al., 2014). During AHPs there is a continent-wide increment in vegetation, closely approaching the Northern Tropic ($23.4°$ N) and effectively shrinking the Sahara (Fig. 3b–e). The largest changes occur around the Sahel, within $10°$ N to $20°$ N, with over 40% increments (Fig. 3f–i). The smallest changes seem to be cornered in northeastern Sahara. Near the equator, in places where
210   there is already close to 100% vegetation cover under pre-industrial forcing, there are also small or no changes during AHPs.

AHP patterns in Fig. 3b–e seem to become weaker sequentially, having the most intense changes during the AHP of MIS 5e on the left, followed by two relatively weaker intermediate cases, and ending with the mildest AHP case during the Holocene (near $10\,\mathrm{ka}$ during MIS 1) on the right. Most apparent is the fading of intense changes around the Sahel, as well as a less pronounced northward push along the west coast. Such step-wise (ignoring long time gaps between AHPs) weakening of
215   AHPs is also evident in the average vegetation fraction in the Sahara (see Fig. 2e). Incremental change occurs in the same direction as the orbital forcing (see Fig. 1a), therefore suggesting the possibility of a linear scaling of a baseline pattern with climate forcing variables. In the following section we explore such linear relationship for vegetation cover fractions.

3.3 Spatio-temporal analysis

AHPs seem quasi-periodic in response to natural rhythms of the Earth system. Possibly there are preferred modes (patterns)
220   of AHP variability (i.e. climate and biogeographies) that regularly appeared in the past during AHP development. In such case it may be assumed that the broadest patterns would tend to scale proportionally to large-scale climate forcing conditions. We investigate this possibility of pattern scaling in the simulated vegetation fractions in North Africa during the last glacial cycle, with the main focus on the potential to capture with this method the simulated AHP patterns of Fig. 3.

We find a baseline pattern of North African vegetation cover variability with an analysis of empirical orthogonal functions
225   (EOFs) and their related principal components (PC) for the entire last glacial cycle. In the analysis the AHPs are simply the cases of maximum possible vegetation coverage. For this we construct a covariance matrix with changes from PI of annual maximum vegetation cover fraction for grid cells inside North Africa ($m = 126$) at centennial temporal resolution ($n = 1340$). The covariance matrix (126×1340) is centred about its mean to remove trends and factorized with a singular value decomposition to obtain its eigenvectors ordered according to explained variance. After decomposition we use only the first eigenvector
230   (EOF_1) which, together with its corresponding time series (PC_1), explains the greatest variability.

Figure 4 shows the results of the EOF analysis. The dominant pattern of variability (EOF_1) explains about 73% of the variance in vegetation fraction changes (Fig. 4a). It is a mostly zonally coherent pattern with an action centre largely inside
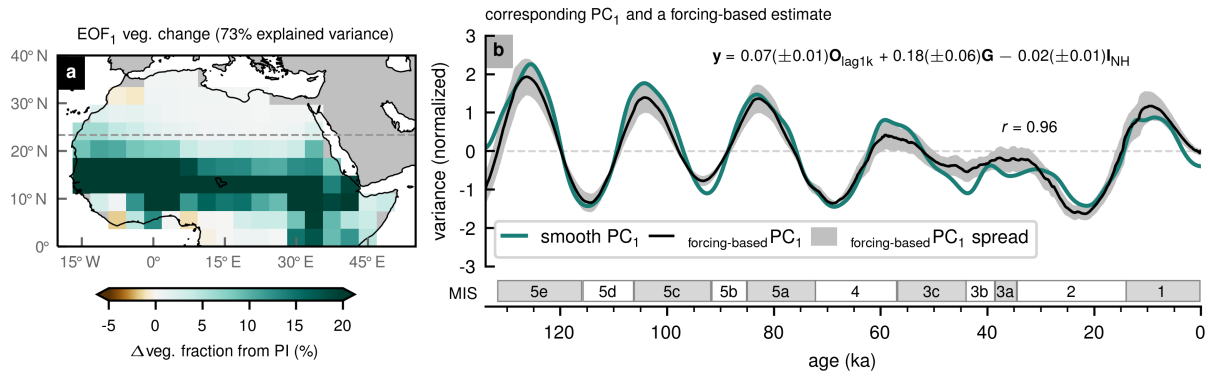
Figure 4. EOF analysis of North African changes in vegetation fraction from pre-industrial (PI) era: (a) leading variability mode (EOF$_1$) and (b) corresponding PC$_1$ time series scaled to unit variance. PC$_1$ is smoothed with a third-order low-pass Butterworth filter with a cutoff frequency of $1/5\,\mathrm{kyr}^{-1}$. (b) includes also a forcing-based estimate for the smooth PC$_1$ (central trend and spread due to uncertainty of regression parameters in parentheses) whose linear regression model equation is shown, where: $\mathbf{O}_{lag1k}$ is orbital forcing monsoon index lagged 1 kyr (cf. lag in Fig. 2e), **G** stands for GHG radiative forcing change from PI, and $\mathbf{I}_{NH}$ is ice-sheet volume in the Northern Hemisphere. Modern coastlines are shown in (a).

$10°$ N to $20°$ N. Near eastern Africa the pattern adopts a more meridional structure, between $30°$ E to $45°$ E. According to its corresponding PC$_1$ (smoothed in Fig. 4b) this mode is related to uniform changes in vegetation fraction with respect to pre-industrial conditions, which are positive and of great amplitude usually during warm interstadials (shaded MIS boxes). PC$_1$ also seems in phase with the orbital forcing monsoon index (compare Fig. 1a). The phasing with the monsoon index is a good indicator of the possibility of estimating PC$_1$ as a function of external climate forcing.

Figure 4b also shows a linear model that combines the orbital monsoon index (lagged 1 kyr and symbolized as O$_{lag1k}$), the GHG radiative forcing (symbolized as G), and the Northern Hemisphere ice-sheet volume (symbolized as I$_{NH}$). The model is fit to the smooth PC$_1$ using an ordinary least-squares method. We choose to lag the orbital monsoon index as a predictor because of the lag in the vegetation peaks explained in Section 3.2.1. Fitting is done several times in different parts of the time series, using a sliding (every $10\,\mathrm{kyr}$) window of $63\,\mathrm{kyr}$ (about three precession cycles), which explains the uncertainty in the regression parameters.

Overall, the linear model ($_{\mathrm{forcing\text{-}based}}PC_1$ in Fig. 4b) estimates a similar trend to the smooth PC$_1$, with some uncertainty in the parameters that leads to some spread. It is possible that other more complicated fits could reproduce the smooth PC$_1$ pattern better, or with less spread, but we restrict our analysis to the simplest fit. In the linear equation it is interesting to note that for the last glacial cycle the standard deviation of O$_{lag1k}$ is close to $10.1\,\mathrm{W\,m}^{-2}$, while that of G is around $0.8\,\mathrm{W\,m}^{-2}$, and that of I$_{NH}$ around $11.0 \times 10^6\,\mathrm{km}^3$. Multiplying these values by the absolute value of their respective fit parameters (0.07, 0.18 and 0.02), it shows that orbital, GHG and ice-sheet variables influence about $66\,\%$, $13\,\%$, and $21\,\%$, respectively, of the outcome of

the linear model. The dominance of the orbital forcing is likewise clearly visbile in the oscillating shape of the linear fit. The

250 fitting seems to perform most poorly after $60\,\mathrm{ka}$, when the orbital forcing becomes much weaker.

3.4 Pattern scaling

We can use the results of the previous section to obtain forcing-based estimates of the vegetation changes (relative to PI) in North Africa. Our method resembles a pattern scaling, where an invariant spatial pattern is assumed to scale linearly with a

255 known forcing factor. The relationship to the climate forcing is based on the curve fit to the smooth PC_1 time series in Fig. 4b, using the linear sum of the orbital monsoon index (lagged $1\,\mathrm{kyr}$), GHG radiative forcing and Northern Hemisphere ice-sheet volume. Because of the use of the principal component time series, another name for this method is also principal component emulator (Wilkinson, 2010), which has been used before also in palaeo-climate modelling contexts (e.g. Holden et al., 2019). Using EOF_1 and $_{\text{forcing-based}}PC_1$ we can approximate mean vegetation changes having forcing variables as predictors. We are

260 especially interested in estimating the mean changes during AHPs.

In Fig. 5 we evaluate the skill of the pattern scaling to predict the simulated vegetation changes (from PI) during the same AHP time slices of Fig. 3. This means the climate model output is acting as reference and errors come from scaled minus simulated fields. We find that for the AHPs of MIS 5 (Fig. 5a, b, and c) the pattern scaling underestimates the vegetation changes inside the Sahara, which is most noticeable in western Africa. Only for the Holocene (Fig. 5d) there is a slight

265 overestimation of vegetation growth during the AHP. That our approach projects only limited changes in the Sahara (e.g. north of $20°\,\mathrm{N}$) is expected because the EOF_1 pattern (Fig. 4b) has more pronounced loadings in the Sahel (near $15°\,\mathrm{N}$). We found other EOF patterns (not shown) that could have provided more changes in the Sahara, however, their associated temporal patterns were not simple to link to the external climate forcing. Nonetheless, considering the magnitude of some of the changes in North Africa whole (above $+40\,\%$ in Fig. 3), root-mean-square errors (RMSE) below $\pm10\,\%$ vegetation cover change in

270 Fig. 4a–d may be seen as acceptable.

Furthermore, Fig. 5e shows the average performance of the pattern scaling. We find the similar outcome that the method predicts intermediate values between the rather-strong AHPs during MIS 5 and the weaker Holocene AHP. We hypothesize that if there had not been the unexpectedly strong AMOC variability during the early Holocene (also seen in Fig. 5e), which weakened the Holocene AHP, our method would find a curve fit able to predict slightly larger values, closer to those during

275 MIS 5. It is also interesting to see that the scaling spread, due to uncertain regression parameters, keeps the climate simulation largely within the reach of the pattern scaling.

3.5 Late Quaternary AHPs

The pattern scaling method opens an interesting possibility to quickly obtain a rough estimate of the vegetation fraction distribution in much of North Africa for other times for which reliable forcing data are available (and yet may lie outside of current

280 modelling capabilities). It seems best suited for the Sahelian vegetation response (where the main loading of the EOF pattern
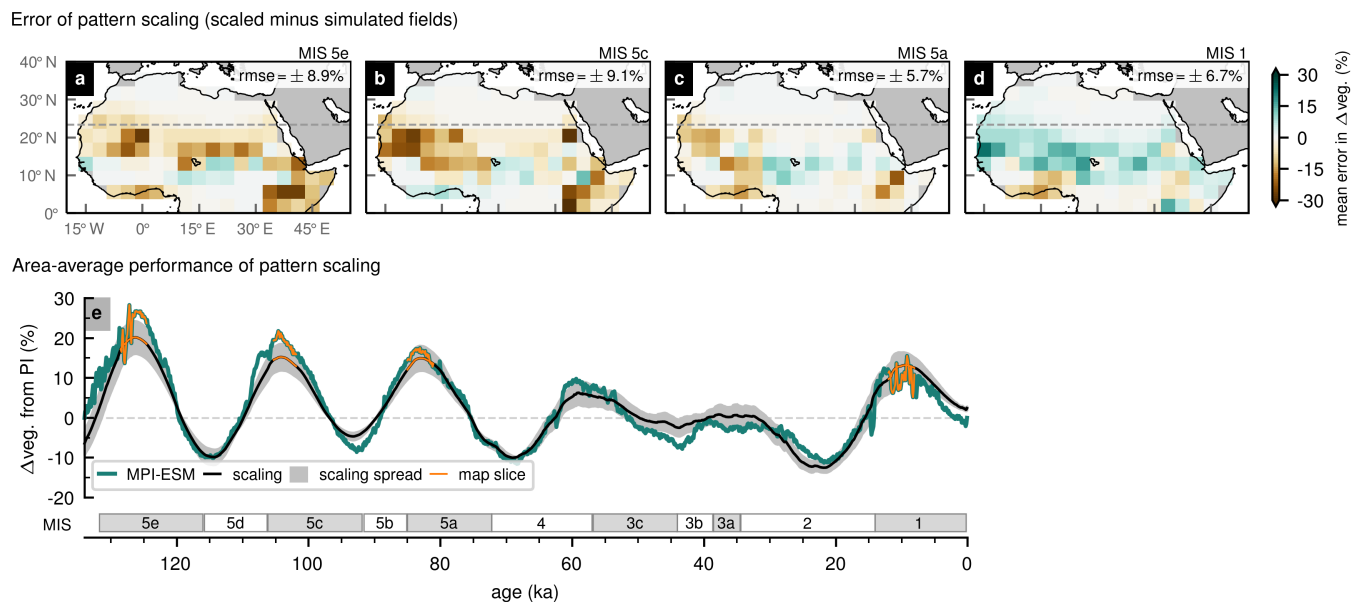
Figure 5. Assessment of pattern scaling method for estimation of change in vegetation fraction from pre-industrial (PI) era: (a–d) mean spatial errors during the AHP time slices highlighted in (e); and (e) domain-wide average performance. This assessment uses the MPI-ESM simulated output as a reference (i.e. errors are scaled minus simulated patterns). In (a–d) the root-mean-square errors (RMSE) are shown. Maps include modern coastlines only as a spatial reference.

lies), however, it still provides part of the vegetation change everywhere in North Africa (e.g. the Sahara), like a minimum probable estimate of the change. Two main assumptions underlying this approach are that (1) the EOF_1 pattern captures much of the large-scale pattern of regional variability, and (2) the forcing-based linear model effectively emulates the long-term time-dependence of variation at that scale and the climate forcing. Although it may likely be biased towards a single glacial cycle, proxy data suggests the last glacial cycle could be representative of large-scale climate changes happening for at least the last eight glacial cycles (Lüthi et al., 2008). Therefore, it is plausible that the pattern scaling generalizes to multiple other cycles.

We use the scaling approach to estimate changes in North Africa since $800\,\mathrm{ka}$ using available forcing data. The orbital monsoon index is computed for this interval based on the parameters of Berger (1978). The GHG radiative forcing and ice sheets data come from Ganopolski and Calov (2011), who compiled the trace gas data from Antarctic ice core records (Petit et al., 1999; EPICA Community Members, 2004), and simulated the ice sheets with a coupled intermediate complexity model and ice-sheet model. Figure 6a–c shows this longer set of forcing variables, where the new GHG and ice sheets data agree with the forcing used in our simulation and to fit the linear model for the overlapping period of the last $134\,\mathrm{kyr}$. In Fig. 6a we also show, as a guide, the orbital monsoon index threshold at $19.8\,\mathrm{W\,m^{-2}}$, which relates to occurrence of AHPs as detected by Rossignol-Strick (1983) and discussed more recently in Duque-Villegas et al. (2022).
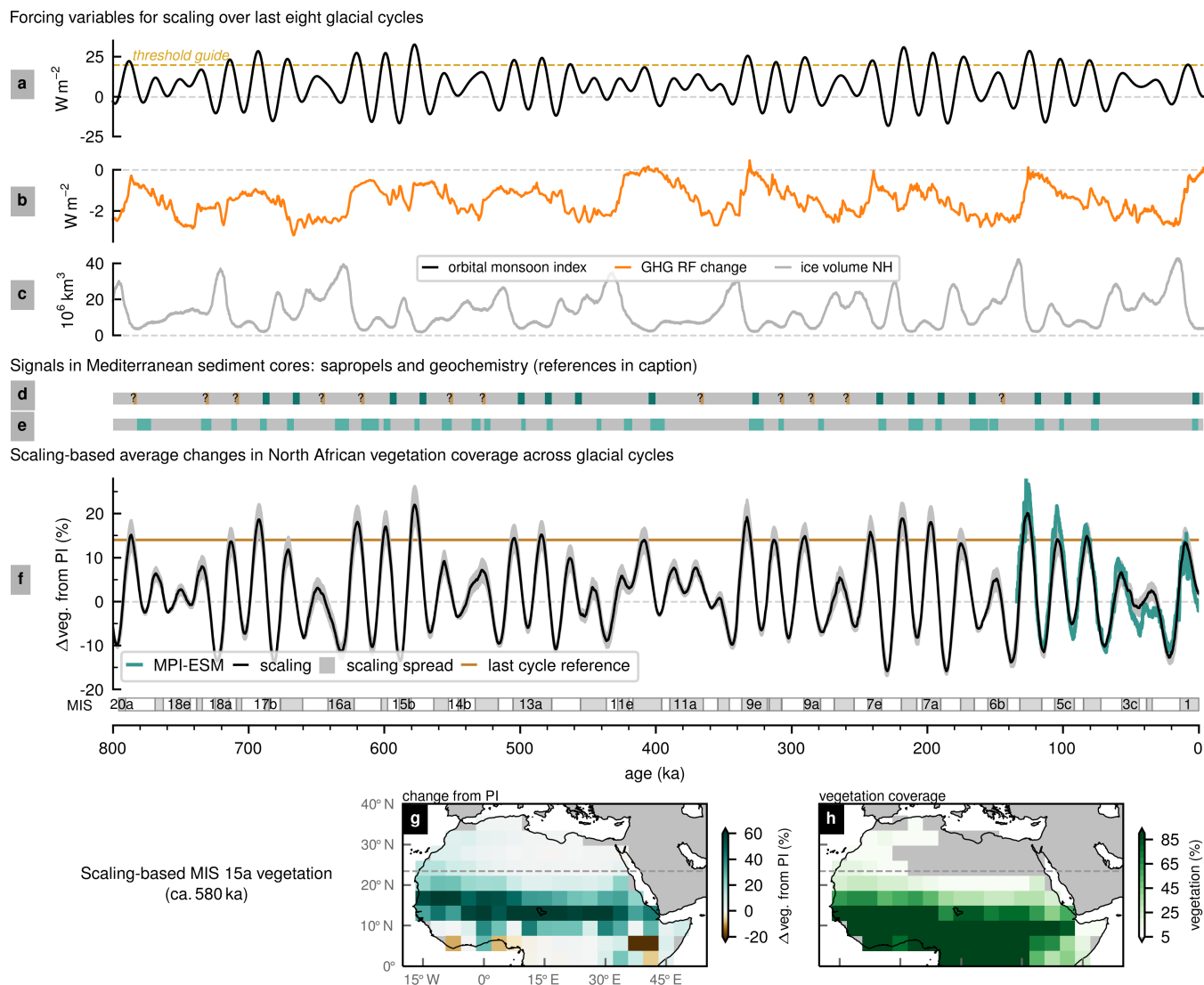
Figure 6. North African vegetation fraction changes over the last $800\,\mathrm{kyr}$. (a–c) set of forcing factors used for scaling, including in (a) the Rossignol-Strick (1983) threshold for sapropel formation at $19.8\,\mathrm{W\,m^{-2}}$; (d) composite sapropel record (cores ODP160-966/7), with wide dark bands for clear sapropels and narrow light bands for oxidized or missing sapropels (Emeis et al., 2000). (e) inferred AHPs (colour bands) from bulk elements in sediments core ODP160-967 (Grant et al., 2022). (f) pattern scaling results for area average changes from pre-industrial (PI) era. A horizontal line at $14\,\%$ is an empirical threshold for counting potential AHPs based on AHPs of the last glacial cycle. (g, h) scaled patterns during potential ancient AHP of MIS 15a, showing modern coastlines even though they may differ at that time.

Evidence of the AHPs of the last $800\,\mathrm{kyr}$ is available in marine proxies. Figure 6d and e depict Mediterranean proxy records linked to past AHPs: the sapropel record of Emeis et al. (2000) and the bulk composition elements in the sediments core of

Grant et al. (2022), respectively. Both long records agree for many events, although the geochemical analysis of Grant et al. (2022) detects several more AHPs. We compare such records with our simulation and pattern scaling approach.

300   Figure 6f shows the last eight glacial cycles of average vegetation changes in North Africa according to the pattern scaling, according to the forcing variables shown in Fig. 6a–c. Figure 6f, also includes a reference line set at 14% of average vegetation change, based on the AHPs of the last glacial cycle, which is useful to guess potential more ancient AHPs. According to this reference guide two other potential AHPs stand out, possibly similarly as strong as the AHP during MIS 5e: one happening around $580\,\mathrm{ka}$, within MIS 15a, and another one near $330\,\mathrm{ka}$, within MIS 9e. The Mediterranean records also clearly contain
305   these two events (Fig. 6d and e).

    The average vegetation changes in Fig. 6f also compare well with the BIOME4 dataset generated with the statistical method in Krapp et al. (2021), although the reconstructed spatial patterns have differences in the zonal extent of the changes (not shown). Moreover, Figure 6g and h show the estimated changes from PI and vegetation fraction pattern, respectively, during one of the potentially strongest AHPs (near $580\,\mathrm{ka}$). It is only one example of the pattern scaling for beyond-simulated AHPs.
310   When considering such an ancient AHP caution is important and it is useful to know, for instance, that the land-sea mask and topography may differ from the one used to calculate the EOF_1 pattern.

    Based on the empirical threshold line in Fig. 6f, the scaling approach can identify most clearly some 19 (potential and known) AHPs. This number agrees with the 21 possible AHPs based only on the orbital monsoon index threshold (see Fig. 6a) detected by Rossignol-Strick (1983). Considering the spread in the parameters of the linear fit, the number could be as
315   low as eight (including the Holocene AHP despite its minimum spread value being under the empirical threshold) or as high as 21 (like the monsoon index threshold would predict). All 21 of the candidate AHPs would be in agreement with signals in Mediterranean sediment cores (combining Fig. 6d and e), neglecting small lags between monsoon index peaks and sedimentary signals. A similar amount of 20 AHPs was reported from many independent equilibrium simulations along this time range (Armstrong et al., 2023). Likewise, a data synthesis by Larrasoaña et al. (2013) indicated 22 potential AHPs for this interval.
320   The refined geochemical analyses by Grant et al. (2022) which read subtle humidity variations estimated about 30 episodes of Saharan greening since $800\,\mathrm{ka}$ (see Fig. 6e). However, some of the events could perhaps be grouped into single cases of AHPs.

3.6   Future AHPs

Previous studies pointed out the differences between orbitally dominated AHPs in the past, and predicted, GHG-modulated, AHPs in the future (Claussen et al., 2003; D'Agostino et al., 2019; Duque-Villegas et al., 2022). For the next $100\,\mathrm{kyr}$ Earth
325   keeps a low eccentricity orbit (a cycle of about 400-kyr) that hinders the possibility of a new AHP inception. At most there could be some mild greening in North Africa near $66\,\mathrm{kyr}$ into the future (Duque-Villegas et al., 2022). The low eccentricity reflects in the small variation in the orbital monsoon index in Fig. 7a, which stays far from the threshold of about $19.8\,\mathrm{W\,m^{-2}}$ for the onset of an AHP detected by Rossignol-Strick (1983) and Duque-Villegas et al. (2022) (compare Fig. 7a with Fig. 6a). However, when compounded with increasing emission rates of GHG, the strengthening of the planetary radiative forcing
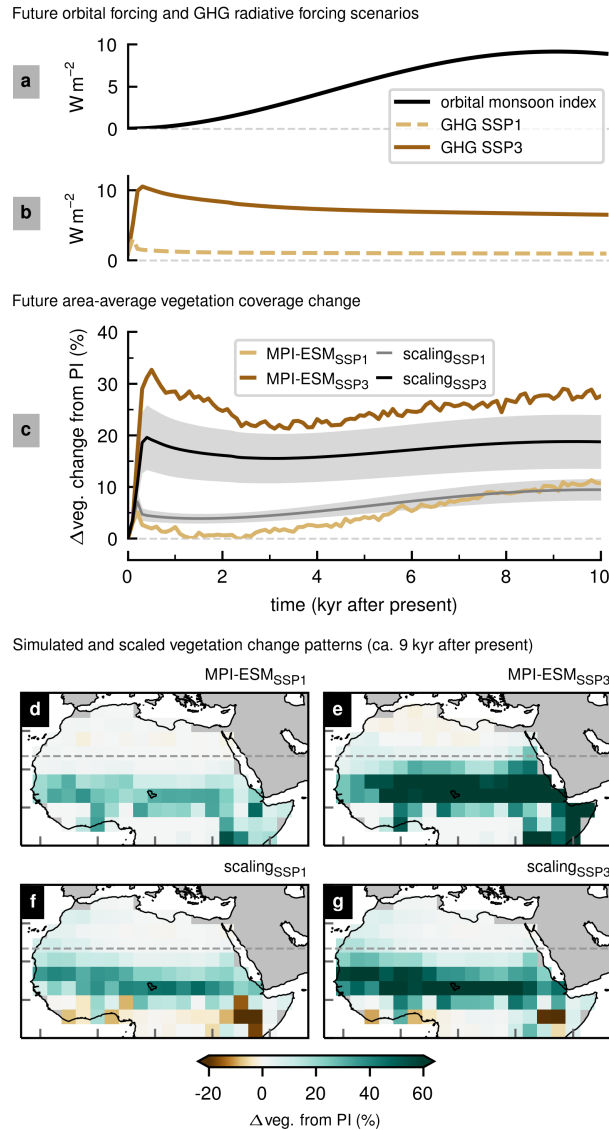
Figure 7. Future vegetation coverage change in North Africa: (a) orbital forcing monsoon index and (b) GHG radiative forcing scenarios; (c) simulated and scaling-based average vegetation fraction change from pre-industrial (PI) era, where grey bands show the scaling spread; and (d, e) mean simulated and (f, g) scaling-based vegetation fraction under forcing scenarios near 9 kyr after PI.

330 (as shown for scenarios in Fig. 7b) enhances humidity levels globally, possibly enabling an earlier greening in North Africa (Duque-Villegas et al., 2022).

Scenarios in Fig. 7b have peak emissions in the near future (a few centuries) and later maintain a constant positive forcing, leading to an average global warming of about 7 K (SSP3) and 1 K (SSP1). Figure 7c shows simulated North African vegetation

response to those scenarios. SSP3 seems to arrive at AHP conditions with a similar level as during MIS 5e (about $30\,\%$ average change from PI), while SSP1 at about $10\,\%$ average vegetation change (which is smaller than during the Holocene) does not resemble an AHP (note the threshold at $14\,\%$ in the previous section).

Figure 7c also shows the average performance of the pattern scaling for future times. It performs relatively well for the SSP1 scenario, but it greatly underestimates the SSP3 changes (even considering the parameter spread). This means the method is rather conservative in terms of the GHG forcing, which could be related to the fitting being done within the narrow range of GHG variability of the last $134\,\mathrm{kyr}$, or because the model includes also the glacial changes in the ice sheets, which for these future scenarios are assumed to remain invariant at present-day conditions. Moreover, our estimate method is bound to the EOF_1 pattern, which means it is not suited to account for greening related to possible future shifts in vegetation boundaries.

Figure 7d–g shows the patterns of vegetation change (from PI) that were dynamically simulated (with MPI-ESM), as well as those estimated with the pattern scaling, near the orbital monsoon index local maximum at $9\,\mathrm{kyr}$ after present. This local maximum in tropical insolation could see substantial greening in North Africa, potentially developing the next AHP, depending on the GHG forcing. Under the relatively low GHG forcing scenario SSP1, the pattern scaling (Fig. 7f) performs well in comparison to MPI-ESM (Fig. 7d). However, Fig. 7e shows that under the high GHG forcing scenario SSP3, the simulated vegetation change pattern differs from its AHP predecessors, since it is missing the northward vegetation push along the west coast. Such difference agrees with first-order effects seen in previous comparisons of climate change projections and the Holocene AHP (e.g. Gaetani et al., 2017; D'Agostino et al., 2019), although such studies did not extend until $9\,\mathrm{kyr}$ after present. Evidently, our single-EOF pattern scaling approach by design lacks in skill to predict vegetation patterns simulated under high GHG forcing, since it is based only on late Quaternary vegetation changes.

4 Discussion

We present results of a coupled atmosphere-ocean-vegetation simulation for the last glacial cycle. To the best of our knowledge, the simulation is unique regarding model complexity, length and the absence of any acceleration technique. Other studies with similar times of interest opted for atmosphere-only models (Prell and Kutzbach, 1987), lesser complexity models (Blanchet et al., 2021; Menviel et al., 2021; Duque-Villegas et al., 2022), ensembles of discontinuous equilibrium simulations (Singarayer and Burrough, 2015; Armstrong et al., 2023), or acceleration methods (Kutzbach et al., 2008, 2020). In this case the simulation includes a realistic representation of interactions across a broad spectrum of variability frequencies, which means disturbances can propagate across the globe to superimpose climate forcing and local effects. However, for the same reason it is not possible to implement a highly resolved grid in this long palaeo-experiment, which would enable a more refined comparison with the geological record and would more clearly capture shifts of vegetation boundaries (e.g. Dallmeyer et al., 2020).

We focus our analysis on vegetation cover in North Africa, where continental-scale climate changes produce four AHPs and a northward greening reaching into the Sahara. The simulated vegetation changes generally agree with timing and direction of change seen in available terrestrial and marine proxies (Blome et al., 2012; Drake et al., 2013; Tierney et al., 2017a; Skonieczny

et al., 2019; Ehrmann and Schmiedl, 2021). However, we detect a dry bias in the model that means Saharan greening is likely underestimated in our simulations. Most of the simulated greening happens within the Sahel region. Especially for the Holocene AHP vegetation cover appears largely underestimated in our simulation, because of unexpectedly large AMOC fluctuations, which resulted in a much colder North Atlantic and Northern Hemisphere while this AHP developed. Nonetheless, we keep
370   this weakened Holocene AHP in our analyses because we still see considerable North African greening, even if only for a few centuries.

Compared with previous modelling and reconstruction studies, the pattern of vegetation changes of the four simulated AHPs seems also consistent with recognized aspects of the Holocene AHP (Brierley et al., 2020; Dallmeyer et al., 2020). There is a northward progression of mostly zonal vegetation bands that extend east until about $40°$ E, with a slight northwest–southeast
375   tilt related to further inland penetration of the West African monsoon system. A "tilted" AHP development pattern is also detected in the simulations and reconstructions of Armstrong et al. (2023), and our results agree about the possibility that desert cover remains during AHPs in a northeastern corner of North Africa, thereby breaking the zonal pattern of northward vegetation growth. Moreover, it was shown that palaeo-conditioning or re-tuning a climate model to improve palaeo-modelling results also led to a similar tilted vegetation pattern during the Holocene (Hopcroft and Valdes, 2021). In our case, however,
380   such tuning is not applied.

Nevertheless, we also see differences with some of the few available sources that include not only the AHP of the Holocene, but also that of MIS 5e. The reconstructions of Larrasoaña (2021) show much more extensive greening of North Africa and a more zonal pattern than our simulation. Also for the AHP of MIS 5e we are unable to simulate enough greening inside the Sahara which would better fit the precipitation changes in the model–data comparison of Scussolini et al. (2019). We believe
385   that part of the reason why these differences stand out is the dry bias in the model at the implemented resolution, but it is also possible that uncertainties and the sparse coverage in the geological record skew the reconstructions (see Otto-Bliesner et al., 2021).

Besides producing and evaluating vegetation patterns for the AHPs of the last glacial cycle, a most interesting outcome is the linear relationship we establish for simulated vegetation in North Africa and the climate drivers forcing the simulations.
390   We had found such a strong correlation previously, but with a different climate model of intermediate complexity, and only for Saharan greening (Duque-Villegas et al., 2022). Similar to our previous work, the dominance of the orbital forcing is clear in our results, yet now with the more comprehensive model we are able to extend this dependence also to the spatial pattern predicted over North Africa by the dynamical model, via a simple linear scaling. The result is a cost-efficient estimation of North African vegetation patterns for the late Quaternary, since simulating glacial cycles even at coarse resolution can take
395   excessively long computing times.

We can compare the results of our pattern scaling with the global biomes dataset generated by Krapp et al. (2021) for the last $800\,\mathrm{kyr}$. In Krapp et al. (2021), authors also use model output for the last glacial cycle to create a linear regression model that can extend simulated variables much further back in time until $800\,\mathrm{ka}$. Similarly, the predictor variables are forcing terms like orbital parameters and atmospheric CO_2. However, in that case the approach was implemented globally and the estimated

changes in North Africa seem more zonal in comparison to our results. Nonetheless, the average evolution of total vegetation changes (one minus the fraction of desert plus barren biomes) agrees well with the domain-average performance of our method, although the estimated number of AHPs seems to be lower in their case.

An important caveat must be considered in our pattern scaling of vegetation fraction. Because this quantity is bounded (0 % to 100 %), it can happen that in some cases the scaling "overshoots" the estimation of the changes, since there is some maximum possible amount of change (from PI) leading to completely bare (0 %) or vegetated (100 %) grid cells. Overshooting could happen, for instance, under more intense forcing (than in the last glacial cycle), or in case there is a greater sensitivity to the forcing. This implies the linear scaling may work well for vegetation fraction in this study only because of a dry bias in the model that prevents simulation of stronger (non-linear) greening.

Another factor we neglect in the scaling approach is the role of non-linear effects. Critical thresholds related to the climate forcing may prevent the pattern scaling approach from correctly representing parts of the changes in the domain (Brovkin et al., 1998; Claussen et al., 2003; Duque-Villegas et al., 2022), most likely near transition zones like around the southern fringe of the Sahara or where there is steep topography like towards eastern Africa. Those are some of the places that stand out when we assess the errors in the pattern scaling (see Fig. 5). Moreover, the dynamical systems that govern North African moisture changes are connected via Walker and Hadley circulations with remote locations whose response to changes in the background climate also could induce more or less greening during simulated AHPs (e.g. Kaboth-Bahr et al., 2021). In this case we have not looked into such tele-connection mechanisms. Although it is possible that some of the other coherent modes of variance improve our estimates (i.e. reduce emulation minus simulation differences), we opt for the simplicity of capturing only the variance at the largest scales, at the cost of a mean error of about $\pm 10 \%$ vegetation fraction change. The fact that the dominant EOF explains about 73 % of the simulated variance justifies our uni-modal approach.

In our simulations of millennial-scale future climate change, we see the contrast between GHG-enabled and orbital-driven vegetation patterns of AHPs. The vegetation pattern under high GHG forcing (Fig. 7e) is similar to 21st century projections of Sahel rainfall changes (e.g. Bony et al., 2013; Gaetani et al., 2017). In both cases (high GHG and 21st century projections) the largest positive anomalies concentrate near central and eastern Sahel. However, in our case (high GHG) a key distinction is that the orbital configuration is changed considerably from present-day, thus we see also some vegetation growth in West Africa and approaching the Northern Tropic. Still, the western and northward development of vegetation under high GHG forcing is not as extensive as in the orbital-driven AHPs of the late Quaternary. This is related to the differences in dynamical (circulation) and thermodynamical (water vapour) responses to each of these forcing factors (Claussen et al., 2003; D'Agostino et al., 2019). Such competing effects complicate AHP pattern predictions in future climates.

5 Conclusions

After simulating a realistic climate evolution for the last glacial cycle, we produce new estimates of the vegetation cover patterns during the last four AHPs. A comparison with available data sources from the geological record and relevant modelling studies indicates that the estimated patterns capture reasonably well some known continental-scale features of AHPs. Nevertheless, a

dry bias in the model version at the resolution we use frames our results rather as probable minimum estimates. We reduce the high-dimensionality in the variability of the vegetation cover changes in North Africa to a single dominant pattern that accounts for 73 % of the variations. We find this single dominant pattern correlates well with known forcing variables and we use this linear relationship to approximate to an acceptable extent the simulated vegetation changes of glacial cycles. Considering the high computational costs of running glacial cycle simulations, we think our approach could be used as a quick diagnostic tool for palaeo-vegetation cover in North Africa, which we demonstrate by estimating vegetation cover changes for the last eight glacial cycles with considerable success. Additionally, the extension of our analysis several millennia into the future suggests that patterns of North African greening under projected strong GHG forcing should differ enough from the vegetation patterns of late Quaternary AHPs that it would not be useful to assume a simple linear scaling with climate forcing for predictions.

Code and data availability. Model source code of MPI-ESM is available to the scientific community upon request to MPI-M. Model output data and post-processing Python scripts to reproduce numbers and figures in the manuscript are archived at https://doi.org/10.17617/3. HQTV1J (Duque-Villegas, 2024). The Lisiecki and Raymo (2005) data in Fig. 1d are available at http://lorraine-lisiecki.com/LR04stack.txt. The Deplazes et al. (2013) data in Fig. 1f are available at https://doi.org/10.1594/PANGAEA.815882. The Tierney et al. (2017a) data in Fig. 2a are available at https://doi.org/10.25921/k92a-8583. The Skonieczny et al. (2019) data in Fig. 2b are available as part of the supplementary material in the online publication. The Ehrmann and Schmiedl (2021) data in Fig. 2c are available at https://doi.org/10.1594/PANGAEA. 923491. Fig. 6b includes data from Loulergue et al. (2008), Lüthi et al. (2008) and Schilt et al. (2010) available at https://doi.org/10.25921/ gfsj-jc86, https://doi.org/10.25921/xgzs-gd10 and https://doi.org/10.25921/yxhy-3g37, respectively. The Emeis et al. (2000) data in Fig. 6d are available at https://doi.org/10.1594/PANGAEA.704622. The Grant et al. (2022) data in Fig. 6e are available as part of the supplementary material in the online publication. The Krapp et al. (2021) data used for comparison can be found at https://doi.org/10.17605/OSF.IO/8N43X. The SPOT/PROBA-V/S3-OLCI and GPCP data in Fig. C1 were provided by the ICDC, CEN at Universität Hamburg.

Appendix A: Backwards extension of transient simulation

The complete 134-kyr simulation is mostly a single experiment that was run continuously from 125 ka to 0 ka. This interval is planned for studies about global climate of the last glacial cycle. However, because for this study we are particularly interested in the regional climate of North Africa, we choose to complement this long experiment with another shorter, independent, and overlapping experiment that has an initial date slightly earlier, spanning from 134 ka to 120 ka. We could use this to extend the longer experiment backwards in time. The main reason is to include in our analysis the tropical insolation maximum near 127 ka, which according to available evidence is an important time of extensive humidity over North Africa. We opt for such an extension due to the computational expense and long waiting time (around two years) that it would take to re-run an entirely new simulation. The overlap in the experiments is to measure their level of agreement near a merging point. They should not be drifting away from each other nor at completely different states.

We find the splicing together of both experiments to have only a small consequence, producing a low amplitude change that can be ignored for the study of the long-term climate signals we focus on for the study of AHPs. Figure A1 shows an example

465 of the state evolution of both experiments for one grid cell in a highly variable region in the North Atlantic (Fig. A1a) and at
the centre of our region of interest (Fig. A1b). The experiments are spliced together at 120 ka to produce the long simulation
starting at 134 ka.
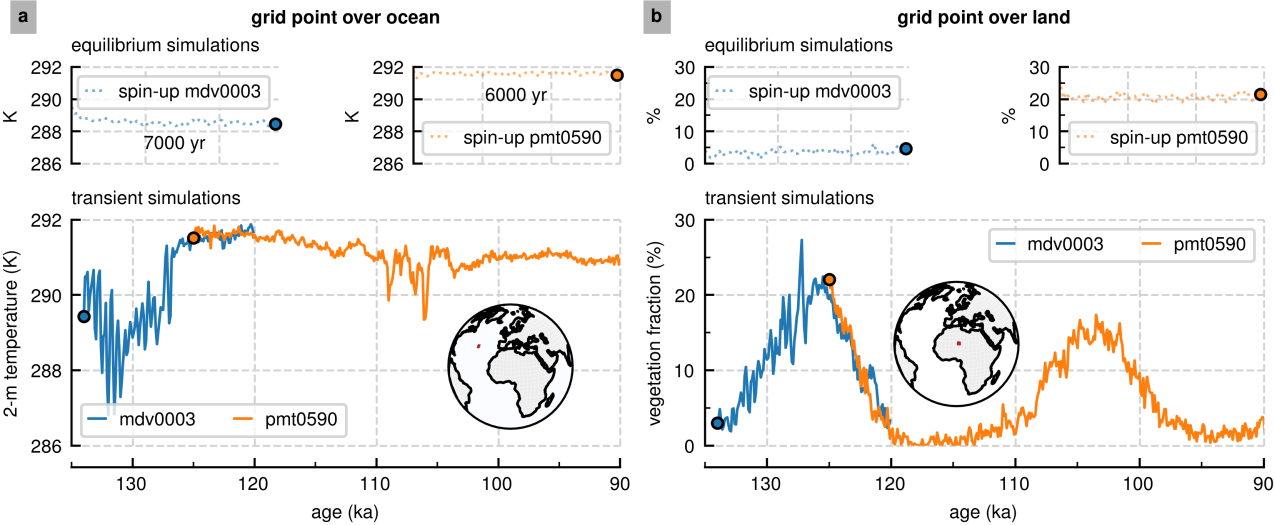
Figure A1. Extending the simulation deeper in time by merging overlapping experiments. Comparison of equilibrium and transient experiments for single grid cells (a) over the North Atlantic (33.75° W 35.26° N) and (b) over land in North Africa (7.5° E 20.41° N). Experiment "mdv0003" spans between 134 ka to 120 ka, while experiment "pmt0590" from 125 ka to 0 ka. We zoom time on the interval close to the merging point. Circle markers show the end state of the equilibrium experiments, also the starting point of the transient experiments.

Appendix B: Background climate near simulated AHPs

To be able to compare more objectively the differences between simulated AHPs we include Fig. B1, where we show the global
470 conditions of near-surface temperature and precipitation near the times of the AHPs. The pre-industrial (PI) conditions (Fig.
B1a), near the year 1850 CE, show the typical poleward temperature gradient profile and the precipitation maximum around
the equator. In Fig. B1b we see the climate during MIS 5e is overall much warmer than during PI, except around the Sahel in
North Africa, where there is more transpiration because of the extended vegetation cover during the AHP. MIS 5c and MIS 5a
show very similar conditions, also with a slightly warmer Arctic Ocean and Siberia regions. In great contrast, the Holocene
475 (MIS 1) shows much colder temperatures over Greenland and the North Atlantic Ocean, due to an excessive amount of sea
ice that remains in this region after a strong meltwater pulse near 14.4 ka. Because of this, the Holocene AHP we present is
not as green as seen in previous applications of the same model at the same spatial resolution. The precipitation changes (Fig.
B1c) show clearly the shift of moisture and ITCZ towards the Northern Hemisphere during the AHPs. The largest increments
in precipitation happen not only in North Africa, but also over the Indian Ocean and over India. Precipitation changes during
480 the Holocene AHP are much weaker than during the other AHPs.
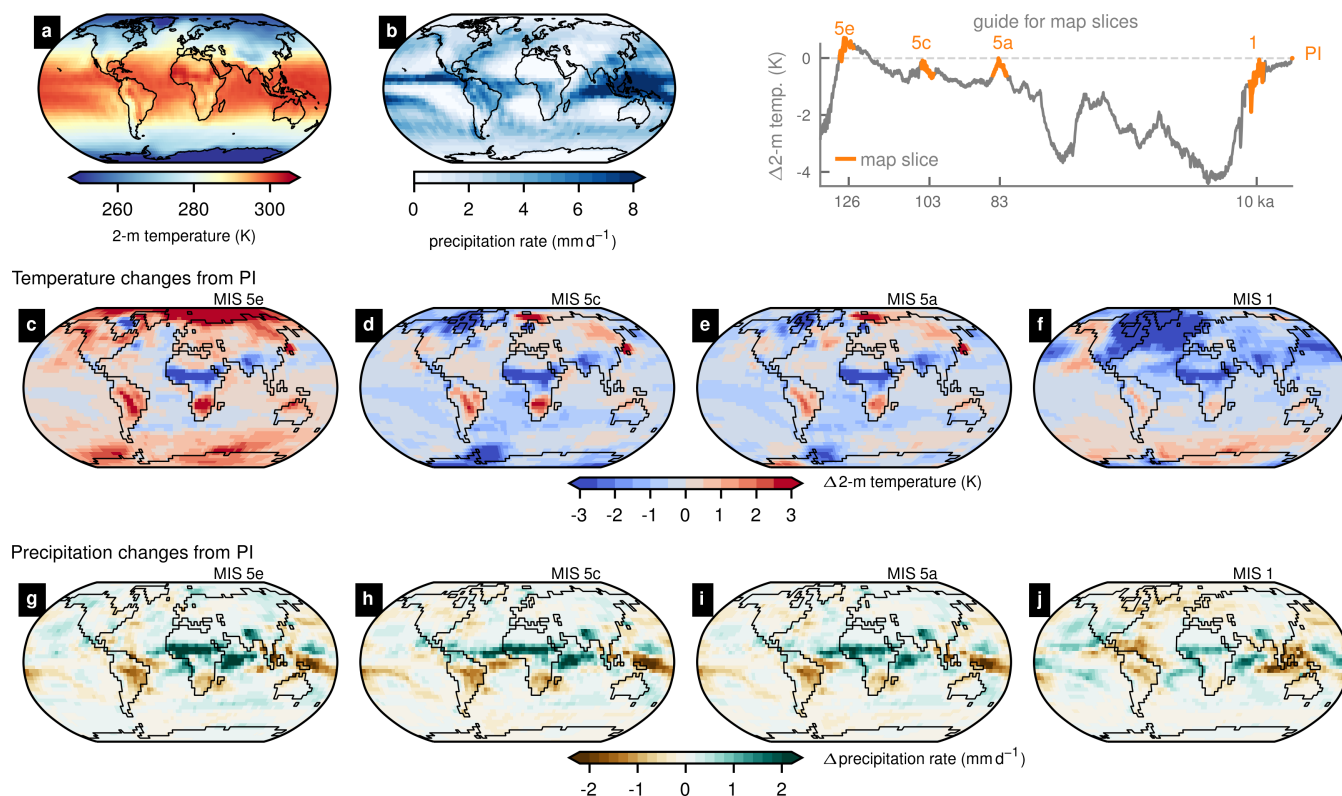
Figure B1. Background climates during AHPs: pre-industrial (PI) era means of (a) near-surface temperature and (b) daily precipitation rate fields; (c–f) temperature changes from PI; and (g–j) precipitation rate changes from PI. Modern coastlines are shown for PI, while AHP time slices show the coastlines according to sea level changes. An inset axes with global mean surface temperature highlights the AHP time slices.

Appendix C: Comparison to present-day observations

For an assessment of the dry bias in this specific implementation of the MPI-ESM model, we also compared the simulated present-day conditions of vegetation cover fractions and precipitation with some observational products in Fig. C1. In this case "present-day" is defined as the climatological mean of 31 years of model output, corresponding to the interval from 1990 CE to 2020 CE. The observational products were remapped to the model grid using a bicubic interpolation and averaged in time to obtain climatologic values. It is important to note that the simulations did not include any anthropogenic land-use changes, therefore, in many places (like near the equator) it is expected that the simulated vegetation cover is an overestimation (potential vegetation cover). Figure C1a–c shows that the patterns of vegetation are similar, but the model underestimated the vegetation cover around the Sahel (in spite of not including land use changes). A dry bias is clearly seen in the precipitation differences in Fig. C1d–f, especially around the Sahel. The large positive anomalies at the equator (almost the only positive anomalies) indicate the maximum of precipitation in the simulation may be displaced southward, relative to the observational product data.
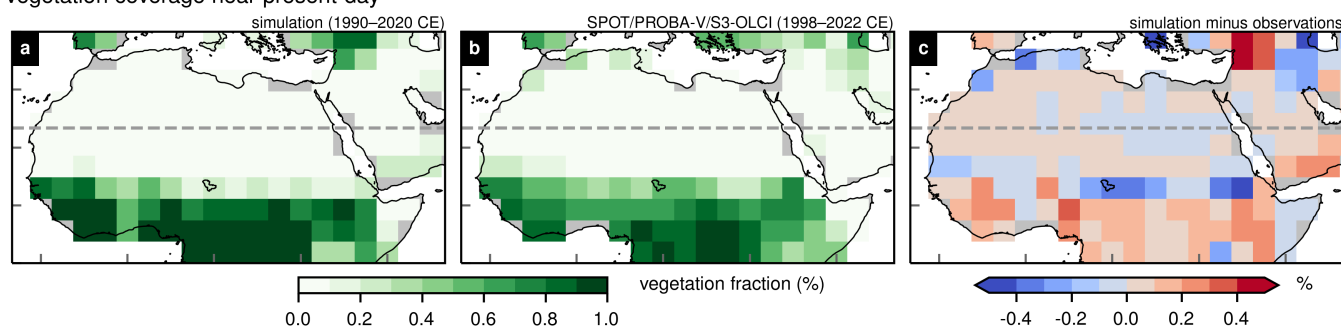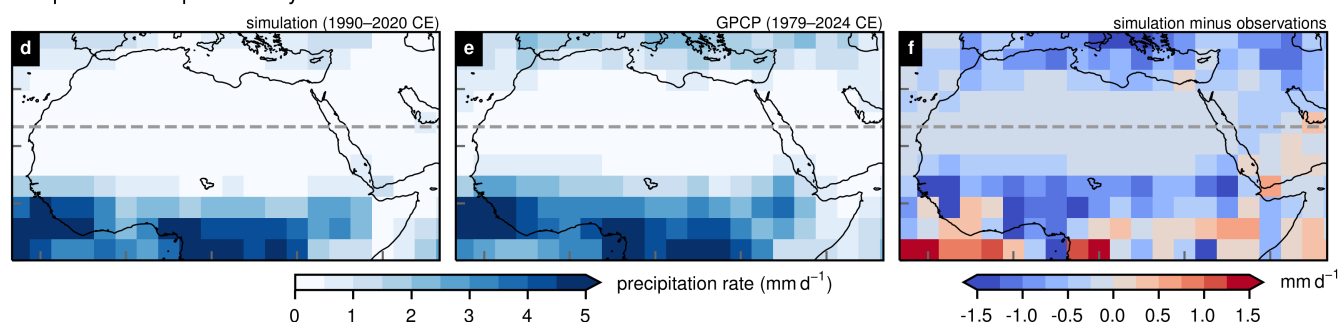
Figure C1. Comparison in North Africa of simulated present-day (1990–2020 CE) conditions to observational products for: (a–c) vegetation cover fractions and (d–f) daily precipitation rates. (b) vegetation cover data are from SPOT/PROBA-V and PROBA-V/S3-OLCI products of the Land Service of Copernicus (Baret et al., 2013; Camacho et al., 2013). (e) precipitation data are from the Global Precipitation Climatology Project (GPCP; Adler et al., 2016).

Author contributions. MDV and MC developed the research idea. MDV and TK performed the climate simulations. MDV led the formal analysis and drafted the manuscript. TK provided model code and input data. JB and CHK contributed to the methodology and formal analysis. All authors participated in the analysis of results and manuscript composition.

495 *Competing interests.* At least one of the (co-)authors is a member of the editorial board of *Climate of the Past*. The authors have no other competing interests to declare.

Acknowledgements. We thank Anne Dallmeyer (MPI-M) for valuable input about an earlier version of the manuscript. Further, we acknowledge the helpful insight from Manuel Chevalier as the handling editor, Shivangi Tiwari and an anonymous referee. Simulations are part of the "PalMod" project, funded by the German Federal Ministry of Education and Research (BMBF) through the Research for Sustainability
500 (FONA) initiative (grant no. 01LP1921A). This work also contributes to the project "African and Asian Monsoon Margins" of the Cluster of Excellence EXC 2037: Climate, Climatic Change, and Society (CLICCS). This work used resources of the Deutsches Klimarechenzen-

trum (DKRZ) granted by its Scientific Steering Committee (WLA) under project ID bm1030. Thanks to the Integrated Climate Data Center (ICDC) of CEN at University of Hamburg for providing data for Fig. C1 via the DKRZ data pool. Analyses and figures were produced using Python, including libraries NumPy, Matplotlib, cartopy, xarray, SciPy, pandas, statsmodels, and cftime.

References

Abe-Ouchi, A., Saito, F., Kawamura, K., Raymo, M. E., Okuno, J., Takahashi, K., and Blatter, H.: Insolation-driven 100,000-year glacial cycles and hysteresis of ice-sheet volume, Nature, 500, 190–193, https://doi.org/10.1038/nature12374, 2013.

Adler, R., Wang, J.-J., Sapiano, M., Huffman, G., Chiu, L., Xie, P. P., Ferraro, R., Schneider, U., Becker, A., Bolvin, D., Nelkin, E., Gu, G., and NOAA CDR Program: Global Precipitation Climatology Project (GPCP) Climate Data Record (CDR), Version 2.3 (Monthly), https://doi.org/10.7289/V56971M6, 2016.

Armstrong, E., Tallavaara, M., Hopcroft, P. O., and Valdes, P. J.: North African humid periods over the past 800,000 years, Nature Communications, 14, 1–11, https://doi.org/10.1038/s41467-023-41219-4, 2023.

Baret, F., Weiss, M., Lacaze, R., Camacho, F., Makhmara, H., Pacholcyzk, P., and Smets, B.: GEOV1: LAI and FAPAR essential climate variables and FCOVER global time series capitalizing over existing products. Part1: Principles of development and production, Remote Sensing of Environment, 137, 299–309, https://doi.org/10.1016/j.rse.2012.12.027, 2013.

Bathiany, S., Claussen, M., and Brovkin, V.: CO2-induced Sahel greening in three CMIP5 Earth System Models, Journal of Climate, 27, 7163–7184, https://doi.org/10.1175/jcli-d-13-00528.1, 2014.

Berger, A.: Long-term variations of daily insolation and Quaternary climatic changes, Journal of the Atmospheric Sciences, 35, 2362–2367, https://doi.org/10.1175/1520-0469(1978)035<2362:LTVODI>2.0.CO;2, 1978.

Blanchet, C. L., Osborne, A. H., Tjallingii, R., Ehrmann, W., Friedrich, T., Timmermann, A., Brückmann, W., and Frank, M.: Drivers of river reactivation in North Africa during the last glacial cycle, Nature Geoscience, 14, 97–103, https://doi.org/10.1038/s41561-020-00671-3, 2021.

Blome, M. W., Cohen, A. S., Tryon, C. A., Brooks, A. S., and Russell, J.: The environmental context for the origins of modern human diversity: A synthesis of regional variability in African climate 150,000–30,000 years ago, Journal of Human Evolution, 62, 563–592, https://doi.org/10.1016/j.jhevol.2012.01.011, 2012.

Bony, S., Bellon, G., Klocke, D., Sherwood, S., Fermepin, S., and Denvil, S.: Robust direct effect of carbon dioxide on tropical circulation and regional precipitation, Nature Geoscience, 6, 447–451, https://doi.org/10.1038/ngeo1799, 2013.

Brierley, C., Zhao, A., Harrison, S. P., Braconnot, P., Williams, C. J. R., Thornalley, D. J. R., Shi, X., Peterschmitt, J.-Y., Ohgaito, R., Kaufman, D. S., Kageyama, M., Hargreaves, J. C., Erb, M. P., Emile-Geay, J., D'Agostino, R., Chandan, D., Carré, M., Bartlein, P. J., Zheng, W., Zhang, Z., Zhang, Q., Yang, H., Volodin, E. M., Tomas, R. A., Routson, C., Peltier, W. R., Otto-Bliesner, B. L., Morozova, P. A., McKay, N. P., Lohmann, G., Legrande, A. N., Guo, C., Cao, J., Brady, E., Annan, J. D., and Abe-Ouchi, A.: Large-scale features and evaluation of the PMIP4-CMIP6 midHolocene simulations, Climate of the Past, 16, 1847–1872, https://doi.org/10.5194/cp-16-1847-2020, 2020.

Briggs, R. D., Pollard, D., and Tarasov, L.: A data-constrained large ensemble analysis of Antarctic evolution since the Eemian, Quaternary Science Reviews, 103, 91–115, https://doi.org/10.1016/j.quascirev.2014.09.003, 2014.

Brovkin, V. and Claussen, M.: Comment on "Climate-driven ecosystem succession in the Sahara: the past 6000 years", Science, 322, 1326–1326, https://doi.org/10.1126/science.1163381, 2008.

Brovkin, V., Claussen, M., Petoukhov, V., and Ganopolski, A.: On the stability of the atmosphere-vegetation system in the Sahara/Sahel region, Journal of Geophysical Research: Atmospheres, 103, 31 613–31 624, https://doi.org/10.1029/1998jd200006, 1998.

Brovkin, V., Raddatz, T., Reick, C. H., Claussen, M., and Gayler, V.: Global biogeophysical interactions between forest and climate, Geophysical Research Letters, 36, 1–5, https://doi.org/10.1029/2009gl037543, 2009.

Brovkin, V., Ganopolski, A., Archer, D., and Munhoven, G.: Glacial CO_2 cycle as a succession of key physical and biogeochemical processes, Climate of the Past, 8, 251–264, https://doi.org/10.5194/cp-8-251-2012, 2012.

Brovkin, V., Boysen, L., Raddatz, T., Gayler, V., Loew, A., and Claussen, M.: Evaluation of vegetation cover and land-surface albedo in MPI-ESM CMIP5 simulations, Journal of Advances in Modeling Earth Systems, 5, 48–57, https://doi.org/10.1029/2012MS000169, 2013.

Camacho, F., Cernicharo, J., Lacaze, R., Baret, F., and Weiss, M.: GEOV1: LAI, FAPAR essential climate variables and FCOVER global time series capitalizing over existing products. Part 2: Validation and intercomparison with reference products, Remote Sensing of Environment, 137, 310–329, https://doi.org/10.1016/j.rse.2013.02.030, 2013.

Claussen, M., Brovkin, V., Ganopolski, A., Kubatzki, C., and Petoukhov, V.: Climate change in Northern Africa: The past is not the future, Climatic Change, 57, 99–118, https://doi.org/10.1023/a:1022115604225, 2003.

Claussen, M., Dallmeyer, A., and Bader, J.: Theory and modeling of the African Humid Period and the Green Sahara, in: Oxford Research Encyclopedia of Climate Science, pp. 1–40, Oxford University Press, https://doi.org/10.1093/acrefore/9780190228620.013.532, 2017.

Crocker, A. J., Naafs, B. D. A., Westerhold, T., James, R. H., Cooper, M. J., Röhl, U., Pancost, R. D., Xuan, C., Osborne, C. P., Beerling, D. J., and Wilson, P. A.: Astronomically controlled aridity in the Sahara since at least 11 million years ago, Nature Geoscience, 15, 671–676, https://doi.org/10.1038/s41561-022-00990-7, 2022.

D'Agostino, R., Bader, J., Bordoni, S., Ferreira, D., and Jungclaus, J.: Northern Hemisphere monsoon response to mid-Holocene orbital forcing and greenhouse gas-induced global warming, Geophysical Research Letters, 46, 1591–1601, https://doi.org/10.1029/2018GL081589, 2019.

Dallmeyer, A., Claussen, M., Lorenz, S. J., and Shanahan, T. M.: The end of the African Humid Period as seen by a transient comprehensive Earth system model simulation of the last 8000 years, Climate of the Past, 16, 117–140, https://doi.org/10.5194/cp-16-117-2020, 2020.

Dallmeyer, A., Kleinen, T., Claussen, M., Weitzel, N., Cao, X., and Herzschuh, U.: The deglacial forest conundrum, Nature Communications, 13, 1–10, https://doi.org/10.1038/s41467-022-33646-6, 2022.

deMenocal, P. B., Ortiz, J., Guilderson, T., Adkins, J., Sarnthein, M., Baker, L., and Yarusinsky, M.: Abrupt onset and termination of the African Humid Period: rapid climate responses to gradual insolation forcing, Quaternary Science Reviews, 19, 347–361, https://doi.org/10.1016/s0277-3791(99)00081-5, 2000.

Deplazes, G., Lückge, A., Peterson, L. C., Timmermann, A., Hamann, Y., Hughen, K. A., Röhl, U., Laj, C., Cane, M. A., Sigman, D. M., and Haug, G. H.: Links between tropical rainfall and North Atlantic climate during the last glacial period, Nature Geoscience, 6, 213–217, https://doi.org/10.1038/ngeo1712, 2013.

Drake, N. A., Blench, R. M., Armitage, S. J., Bristow, C. S., and White, K. H.: Ancient watercourses and biogeography of the Sahara explain the peopling of the desert, Proceedings of the National Academy of Sciences, 108, 458–462, https://doi.org/10.1073/pnas.1012231108, 2011.

Drake, N. A., Breeze, P. S., and Parker, A.: Palaeoclimate in the Saharan and Arabian Deserts during the Middle Palaeolithic and the potential for hominin dispersals, Quaternary International, 300, 48–61, https://doi.org/10.1016/j.quaint.2012.12.018, 2013.

Drake, N. A., Lem, R. E., Armitage, S. J., Breeze, P. S., Francke, J., El-Hawat, A. S., Salem, M. J., Hounslow, M. W., and White, K.: Reconstructing palaeoclimate and hydrological fluctuations in the Fezzan Basin (southern Libya) since 130 ka: A catchment-based approach, Quaternary Science Reviews, 200, 376–394, https://doi.org/10.1016/j.quascirev.2018.09.042, 2018.

Drake, N. A., Candy, I., Breeze, P. S., Armitage, S. J., Gasmi, N., Schwenninger, J. L., Peat, D., and Manning, K.: Sedimentary and geomorphic evidence of Saharan megalakes: A synthesis, Quaternary Science Reviews, 276, 1–20, https://doi.org/10.1016/j.quascirev.2021.107318, 2022.

580 Duque-Villegas, M.: Post-processed data and scripts for "Pattern scaling of simulated vegetation change in North Africa during glacial cycles", Edmond, V1, https://doi.org/10.17617/3.HQTV1J, 2024.

Duque-Villegas, M., Claussen, M., Brovkin, V., and Kleinen, T.: Effects of orbital forcing, greenhouse gases and ice sheets on Saharan greening in past and future multi-millennia, Climate of the Past, 18, 1897–1914, https://doi.org/10.5194/cp-18-1897-2022, 2022.

Ehrmann, W. and Schmiedl, G.: Nature and dynamics of North African humid and dry periods during the last 200,000
585 years documented in the clay fraction of Eastern Mediterranean deep-sea sediments, Quaternary Science Reviews, 260, 1–17, https://doi.org/10.1016/j.quascirev.2021.106925, 2021.

Ehrmann, W., Schmiedl, G., Beuscher, S., and Krüger, S.: Intensity of African humid periods estimated from Saharan dust fluxes, PloS ONE, 12, 1–18, https://doi.org/10.1371/journal.pone.0170989, 2017.

Emeis, K.-C., Sakamoto, T., Wehausen, R., and Brumsack, H.-J.: The sapropel record of the eastern Mediterranean Sea – results of
590 Ocean Drilling Program Leg 160, Palaeogeography, Palaeoclimatology, Palaeoecology, 158, 371–395, https://doi.org/10.1016/S0031-0182(00)00059-6, 2000.

EPICA Community Members: Eight glacial cycles from an Antarctic ice core, Nature, 429, 623–628, https://doi.org/10.1038/nature02599, 2004.

Eyring, V., Bony, S., Meehl, G. A., Senior, C. A., Stevens, B., Stouffer, R. J., and Taylor, K. E.: Overview of the Coupled Model
595 Intercomparison Project Phase 6 (CMIP6) experimental design and organization, Geoscientific Model Development, 9, 1937–1958, https://doi.org/10.5194/gmd-9-1937-2016, 2016.

Gaetani, M., Flamant, C., Bastin, S., Janicot, S., Lavaysse, C., Hourdin, F., Braconnot, P., and Bony, S.: West African monsoon dynamics and precipitation: the competition between global SST warming and CO2 increase in CMIP5 idealized simulations, Climate Dynamics, 48, 1353–1373, https://doi.org/10.1007/s00382-016-3146-z, 2017.

600 Ganopolski, A. and Calov, R.: The role of orbital forcing, carbon dioxide and regolith in 100 kyr glacial cycles, Climate of the Past, 7, 1415–1425, https://doi.org/10.5194/cp-7-1415-2011, 2011.

Ganopolski, A., Calov, R., and Claussen, M.: Simulation of the last glacial cycle with a coupled climate ice-sheet model of intermediate complexity, Climate of the Past, 6, 229–244, https://doi.org/10.5194/cp-6-229-2010, 2010.

Ganopolski, A., Winkelmann, R., and Schellnhuber, H. J.: Critical insolation–CO_2 relation for diagnosing past and future glacial inception,
605 Nature, 529, 200–203, https://doi.org/10.1038/nature16494, 2016.

Gasse, F.: Hydrological changes in the African tropics since the Last Glacial Maximum, Quaternary Science Reviews, 19, 189–211, https://doi.org/10.1016/s0277-3791(99)00061-x, 2000.

Giorgetta, M. A., Jungclaus, J., Reick, C. H., Legutke, S., Bader, J., Böttinger, M., Brovkin, V., Crueger, T., Esch, M., Fieg, K., Glushak, K., Gayler, V., Haak, H., Hollweg, H. D., Ilyina, T., Kinne, S., Kornblueh, L., Matei, D., Mauritsen, T., Mikolajewicz, U., Mueller, W.,
610 Notz, D., Pithan, F., Raddatz, T., Rast, S., Redler, R., Roeckner, E., Schmidt, H., Schnur, R., Segschneider, J., Six, K. D., Stockhause, M., Timmreck, C., Wegner, J., Widmann, H., Wieners, K. H., Claussen, M., Marotzke, J., and Stevens, B.: Climate and carbon cycle changes from 1850 to 2100 in MPI-ESM simulations for the Coupled Model Intercomparison Project phase 5, Journal of Advances in Modeling Earth Systems, 5, 572–597, https://doi.org/10.1002/jame.20038, 2013.

Grant, K. M., Rohling, E. J., Westerhold, T., Zabel, M., Heslop, D., Konijnendijk, T., and Lourens, L.: A 3 million year index for North
615 African humidity/aridity and the implication of potential pan-African Humid periods, Quaternary Science Reviews, 171, 100–118, https://doi.org/10.1016/j.quascirev.2017.07.005, 2017.

Grant, K. M., Amarathunga, U., Amies, J. D., Hu, P., Qian, Y., Penny, T., Rodriguez-Sanz, L., Zhao, X., Heslop, D., Liebrand, D., Hennekam, R., Westerhold, T., Gilmore, S., Lourens, L. J., Roberts, A. P., and Rohling, E. J.: Organic carbon burial in Mediterranean sapropels intensified during Green Sahara Periods since 3.2 Myr ago, Communications Earth & Environment, 3, 1–9, https://doi.org/10.1038/s43247-021-00339-9, 2022.

Hély, C., Lézine, A.-M., Ballouche, A., Cour, P., Duzer, D., Guinet, P., Jahns, S., Maley, J., Mercuri, A. M., Pons, A., Ritchie, J. C., Salzmann, U., Schulz, E., Campo, M. V., and Waller, M. P.: Holocene changes in African vegetation: tradeoff between climate and water availability, Climate of the Past, 10, 681–686, https://doi.org/10.5194/cp-10-681-2014, 2014.

Holden, P. B., Edwards, N. R., Rangel, T. F., Pereira, E. B., Tran, G. T., and Wilkinson, R. D.: PALEO-PGEM v1.0: a statistical emulator of Pliocene–Pleistocene climate, Geoscientific Model Development, 12, 5137–5155, https://doi.org/10.5194/gmd-12-5137-2019, 2019.

Hopcroft, P. O. and Valdes, P. J.: Paleoclimate-conditioning reveals a North Africa land–atmosphere tipping point, Proceedings of the National Academy of Sciences, 118, 1–7, https://doi.org/10.1073/pnas.2108783118, 2021.

IPCC: Climate Change 2021 – The Physical Science Basis: Working Group I Contribution to the Sixth Assessment Report of the Intergovernmental Panel on Climate Change, Cambridge University Press, Cambridge, United Kingdom and New York, NY, USA, ISBN 9781009157896, https://doi.org/10.1017/9781009157896, 2021.

Jungclaus, J. H., Fischer, N., Haak, H., Lohmann, K., Marotzke, J., Matei, D., Mikolajewicz, U., Notz, D., and von Storch, J. S.: Characteristics of the ocean simulations in the Max Planck Institute Ocean Model (MPIOM) the ocean component of the MPI-Earth system model, Journal of Advances in Modeling Earth Systems, 5, 422–446, https://doi.org/10.1002/jame.20023, 2013.

Kaboth-Bahr, S., Gosling, W. D., Vogelsang, R., Bahr, A., Scerri, E. M. L., Asrat, A., Cohen, A. S., Düsing, W., Foerster, V., Lamb, H. F., Maslin, M. A., Roberts, H. M., Schäbitz, F., and Trauth, M. H.: Paleo-ENSO influence on African environments and early modern humans, Proceedings of the National Academy of Sciences, 118, 1–6, https://doi.org/10.1073/pnas.2018277118, 2021.

Kapsch, M.-L., Mikolajewicz, U., Ziemen, F., and Schannwell, C.: Ocean response in transient simulations of the last deglaciation dominated by underlying ice-sheet reconstruction and method of meltwater distribution, Geophysical Research Letters, 49, 1–11, https://doi.org/10.1029/2021gl096767, 2022.

Kinne, S., O'Donnel, D., Stier, P., Kloster, S., Zhang, K., Schmidt, H., Rast, S., Giorgetta, M., Eck, T. F., and Stevens, B.: MAC-v1: A new global aerosol climatology for climate studies, Journal of Advances in Modeling Earth Systems, 5, 704–740, https://doi.org/10.1002/jame.20035, 2013.

Kleinen, T., Gromov, S., Steil, B., and Brovkin, V.: Atmospheric methane underestimated in future climate projections, Environmental Research Letters, 16, 1–12, https://doi.org/10.1088/1748-9326/ac1814, 2021.

Kleinen, T., Gromov, S., Steil, B., and Brovkin, V.: Atmospheric methane since the last glacial maximum was driven by wetland sources, Climate of the Past, 19, 1081–1099, https://doi.org/10.5194/cp-19-1081-2023, 2023.

Köhler, P., Nehrbass-Ahles, C., Schmitt, J., Stocker, T. F., and Fischer, H.: A 156 kyr smoothed history of the atmospheric greenhouse gases CO_2, CH_4, and N_2O and their radiative forcing, Earth System Science Data, 9, 363–387, https://doi.org/10.5194/essd-9-363-2017, 2017.

Krapp, M., Beyer, R. M., Edmundson, S. L., Valdes, P. J., and Manica, A.: A statistics-based reconstruction of high-resolution global terrestrial climate for the last 800,000 years, Scientific Data, 8, 1–18, https://doi.org/10.1038/s41597-021-01009-3, 2021.

Kutzbach, J. E., Liu, X., Liu, Z., and Chen, G.: Simulation of the evolutionary response of global summer monsoons to orbital forcing over the past 280,000 years, Climate Dynamics, 30, 567–579, https://doi.org/10.1007/s00382-007-0308-z, 2008.

Kutzbach, J. E., Guan, J., He, F., Cohen, A. S., Orland, I. J., and Chen, G.: African climate response to orbital and glacial forcing in 140,000-y simulation with implications for early modern human environments, Proceedings of the National Academy of Sciences, 117, 2255–2264, https://doi.org/10.1073/pnas.1917673117, 2020.

Larrasoaña, J. C.: A review of West African monsoon penetration during Green Sahara periods – implications for human evolution and dispersals over the last three million years, Oxford Open Climate Change, 1, 1–19, https://doi.org/10.1093/oxfclm/kgab011, 2021.

Larrasoaña, J. C., Roberts, A. P., and Rohling, E. J.: Dynamics of green Sahara periods and their role in hominin evolution, PLoS ONE, 8, 1–12, https://doi.org/10.1371/journal.pone.0076514, 2013.

Lézine, A.-M., Hély, C., Grenier, C., Braconnot, P., and Krinner, G.: Sahara and Sahel vulnerability to climate changes, lessons from Holocene hydrological data, Quaternary Science Reviews, 30, 3001–3012, https://doi.org/10.1016/j.quascirev.2011.07.006, 2011.

Lisiecki, L. E. and Raymo, M. E.: A Pliocene-Pleistocene stack of 57 globally distributed benthic δ^{18}O records, Paleoceanography, 20, 1–17, https://doi.org/10.1029/2004pa001071, 2005.

Loulergue, L., Schilt, A., Spahni, R., Masson-Delmotte, V., Blunier, T., Lemieux, B., Barnola, J.-M., Raynaud, D., Stocker, T. F., and Chappellaz, J.: Orbital and millennial-scale features of atmospheric CH4 over the past 800,000 years, Nature, 453, 383–386, https://doi.org/10.1038/nature06950, 2008.

Lunt, D. J., Abe-Ouchi, A., Bakker, P., Berger, A., Braconnot, P., Charbit, S., Fischer, N., Herold, N., Jungclaus, J. H., Khon, V. C., Krebs-Kanzow, U., Langebroek, P. M., Lohmann, G., Nisancioglu, K. H., Otto-Bliesner, B. L., Park, W., Pfeiffer, M., Phipps, S. J., Prange, M., Rachmayani, R., Renssen, H., Rosenbloom, N., Schneider, B., Stone, E. J., Takahashi, K., Wei, W., Yin, Q., and Zhang, Z. S.: A multi-model assessment of last interglacial temperatures, Climate of the Past, 9, 699–717, https://doi.org/10.5194/cp-9-699-2013, 2013.

Lüthi, D., Floch, M. L., Bereiter, B., Blunier, T., Barnola, J.-M., Siegenthaler, U., Raynaud, D., Jouzel, J., Fischer, H., Kawamura, K., and Stocker, T. F.: High-resolution carbon dioxide concentration record 650,000–800,000 years before present, Nature, 453, 379–382, https://doi.org/10.1038/nature06949, 2008.

Mauritsen, T., Bader, J., Becker, T., Behrens, J., Bittner, M., Brokopf, R., Brovkin, V., Claussen, M., Crueger, T., Esch, M., et al.: Developments in the MPI-M Earth System Model version 1.2 (MPI-ESM1.2) and its response to increasing CO2, Journal of Advances in Modeling Earth Systems, 11, 998–1038, https://doi.org/10.1029/2018MS001400, 2019.

McGee, D., deMenocal, P. B., Winckler, G., Stuut, J.-B. W., and Bradtmiller, L. I.: The magnitude, timing and abruptness of changes in North African dust deposition over the last 20,000 yr, Earth and Planetary Science Letters, 371, 163–176, https://doi.org/10.1016/j.epsl.2013.03.054, 2013.

Meccia, V. L. and Mikolajewicz, U.: Interactive ocean bathymetry and coastlines for simulating the last deglaciation with the Max Planck Institute Earth System Model (MPI-ESM-v1. 2), Geoscientific Model Development, 11, 4677–4692, https://doi.org/10.5194/gmd-11-4677-2018, 2018.

Meinshausen, M., Nicholls, Z. R. J., Lewis, J., Gidden, M. J., Vogel, E., Freund, M., Beyerle, U., Gessner, C., Nauels, A., Bauer, N., Canadell, J. G., Daniel, J. S., John, A., Krummel, P. B., Luderer, G., Meinshausen, N., Montzka, S. A., Rayner, P. J., Reimann, S., Smith, S. J., van den Berg, M., Velders, G. J. M., Vollmer, M. K., and Wang, R. H. J.: The shared socio-economic pathway (SSP) greenhouse gas concentrations and their extensions to 2500, Geoscientific Model Development, 13, 3571–3605, https://doi.org/10.5194/gmd-13-3571-2020, 2020.

Menviel, L., Capron, E., Govin, A., Dutton, A., Tarasov, L., Abe-Ouchi, A., Drysdale, R. N., Gibbard, P. L., Gregoire, L., He, F., Ivanovic, R. F., Kageyama, M., Kawamura, K., Landais, A., Otto-Bliesner, B. L., Oyabu, I., Tzedakis, P. C., Wolff, E., and Zhang, X.: The penultimate deglaciation: protocol for Paleoclimate Modelling Intercomparison Project (PMIP) phase 4 transient numerical simulations between 140 and 127 ka, version 1.0, Geoscientific Model Development, 12, 3649–3685, https://doi.org/10.5194/gmd-12-3649-2019, 2019.

Menviel, L., Govin, A., Avenas, A., Meissner, K. J., Grant, K. M., and Tzedakis, P. C.: Drivers of the evolution and amplitude of African Humid Periods, Communications Earth & Environment, 2, 1–11, https://doi.org/10.1038/s43247-021-00309-1, 2021.

Mikolajewicz, U., Ziemen, F., Cioni, G., Claussen, M., Fraedrich, K. F., Heidkamp, M., Hohenegger, C., de la Cuesta, D. J., Kapsch, M.-L., Lemburg, A., Mauritsen, T., Meraner, K., Röber, N., Schmidt, H., Six, K. D., Stemmler, I., Tamarin-Brodsky, T., Winkler, A., Zhu, X., and Stevens, B.: The climate of a retrograde rotating Earth, Earth System Dynamics, 9, 1191–1215, https://doi.org/10.5194/esd-9-1191-2018, 2018.

Milankovitch, M.: Kanon der Erdbestrahlung und seine Anwendung auf das Eiszeitenproblem, vol. 33 of *Section des sciences mathémathiques et naturelles*, Königlich Serbische Akademie, Belgrad, 1941.

Osman, M. B., Tierney, J. E., Zhu, J., Tardif, R., Hakim, G. J., King, J., and Poulsen, C. J.: Globally resolved surface temperatures since the Last Glacial Maximum, Nature, 599, 239–244, https://doi.org/10.1038/s41586-021-03984-4, 2021.

Otto-Bliesner, B. L., Brady, E. C., Zhao, A., Brierley, C. M., Axford, Y., Capron, E., Govin, A., Hoffman, J. S., Isaacs, E., Kageyama, M., Scussolini, P., Tzedakis, P. C., Williams, C. J. R., Wolff, E., Abe-Ouchi, A., Braconnot, P., Buarque, S. R., Cao, J., de Vernal, A., Guarino, M. V., Guo, C., LeGrande, A. N., Lohmann, G., Meissner, K. J., Menviel, L., Morozova, P. A., Nisancioglu, K. H., O'ishi, R., y Mélia, D. S., Shi, X., Sicard, M., Sime, L., Stepanek, C., Tomas, R., Volodin, E., Yeung, N. K. H., Zhang, Q., Zhang, Z., and Zheng, W.: Large-scale features of Last Interglacial climate: results from evaluating the lig127k simulations for the Coupled Model Intercomparison Project (CMIP6) – Paleoclimate Modeling Intercomparison Project (PMIP4), Climate of the Past, 17, 63–94, https://doi.org/10.5194/cp-17-63-2021, 2021.

Pausata, F. S. R., Gaetani, M., Messori, G., Berg, A., de Souza, D. M., Sage, R. F., and deMenocal, P. B.: The greening of the Sahara: Past changes and future implications, One Earth, 2, 235–250, https://doi.org/10.1016/j.oneear.2020.03.002, 2020.

Petit, J. R., Jouzel, J., Raynaud, D., Barkov, N. I., Barnola, J.-M., Basile, I., Bender, M., Chappellaz, J., Davis, M., Delaygue, G., Delmotte, M., Kotlyakov, V. M., Legrand, M., Lipenkov, V. Y., Lorius, C., PÉpin, L., Ritz, C., Saltzman, E., and Stievenard, M.: Climate and atmospheric history of the past 420,000 years from the Vostok ice core, Antarctica, Nature, 399, 429–436, https://doi.org/10.1038/20859, 1999.

Prell, W. L. and Kutzbach, J. E.: Monsoon variability over the past 150,000 years, Journal of Geophysical Research, 92, 8411–8425, https://doi.org/10.1029/JD092iD07p08411, 1987.

Railsback, L. B., Gibbard, P. L., Head, M. J., Voarintsoa, N. R. G., and Toucanne, S.: An optimized scheme of lettered marine isotope substages for the last 1.0 million years, and the climatostratigraphic nature of isotope stages and substages, Quaternary Science Reviews, 111, 94–106, https://doi.org/10.1016/j.quascirev.2015.01.012, 2015.

Reick, C. H., Raddatz, T., Brovkin, V., and Gayler, V.: Representation of natural and anthropogenic land cover change in MPI-ESM, Journal of Advances in Modeling Earth Systems, 5, 459–482, https://doi.org/10.1002/jame.20022, 2013.

Riddick, T., Brovkin, V., Hagemann, S., and Mikolajewicz, U.: Dynamic hydrological discharge modelling for coupled climate model simulations of the last glacial cycle: the MPI-DynamicHD model version 3.0, Geoscientific Model Development, 11, 4291–4316, https://doi.org/10.5194/gmd-11-4291-2018, 2018.

Rossignol-Strick, M.: African monsoons, an immediate climate response to orbital insolation, Nature, 304, 46–49, https://doi.org/10.1038/304046a0, 1983.

Scerri, E. M. L., Drake, N. A., Jennings, R., and Groucutt, H. S.: Earliest evidence for the structure of Homo sapiens populations in Africa, Quaternary Science Reviews, 101, 207–216, https://doi.org/10.1016/j.quascirev.2014.07.019, 2014.

Scerri, E. M. L., Thomas, M. G., Manica, A., Gunz, P., Stock, J. T., Stringer, C., Grove, M., Groucutt, H. S., Timmermann, A., Rightmire, G. P., d'Errico, F., Tryon, C. A., Drake, N. A., Brooks, A. S., Dennell, R. W., Durbin, R., Henn, B. M., Lee-Thorp, J., deMenocal, P. B.,

730 Petraglia, M. D., Thompson, J. C., Scally, A., and Chikhi, L.: Did our species evolve in subdivided populations across Africa, and why does it matter?, Trends in Ecology & Evolution, 33, 582–594, https://doi.org/10.1016/j.tree.2018.05.005, 2018.

Schilt, A., Baumgartner, M., Blunier, T., Schwander, J., Spahni, R., Fischer, H., and Stocker, T. F.: Glacial–interglacial and millennial-scale variations in the atmospheric nitrous oxide concentration during the last 800,000 years, Quaternary Science Reviews, 29, 182–192, https://doi.org/10.1016/j.quascirev.2009.03.011, 2010.

735 Scussolini, P., Bakker, P., Guo, C., Stepanek, C., Zhang, Q., Braconnot, P., Cao, J., Guarino, M.-V., Coumou, D., Prange, M., Ward, P. J., Renssen, H., Kageyama, M., Otto-Bliesner, B. L., and Aerts, J. C. J. H.: Agreement between reconstructed and modeled boreal precipitation of the Last Interglacial, Science Advances, 5, 1–11, https://doi.org/10.1126/sciadv.aax7047, 2019.

Shanahan, T. M., McKay, N. P., Hughen, K. A., Overpeck, J. T., Otto-Bliesner, B. L., Heil, C. W., King, J., Scholz, C. A., and Peck, J.: The time-transgressive termination of the African Humid Period, Nature Geoscience, 8, 140–144, https://doi.org/10.1038/ngeo2329, 2015.

740 Singarayer, J. S. and Burrough, S. L.: Interhemispheric dynamics of the African rainbelt during the late Quaternary, Quaternary Science Reviews, 124, 48–67, https://doi.org/10.1016/j.quascirev.2015.06.021, 2015.

Skonieczny, C., McGee, D., Winckler, G., Bory, A., Bradtmiller, L. I., Kinsley, C. W., Polissar, P. J., Pol-Holz, R. D., Rossignol, L., and Malaizé, B.: Monsoon-driven Saharan dust variability over the past 240,000 years, Science Advances, 5, 1–8, https://doi.org/10.1126/sciadv.aav1887, 2019.

745 Stevens, B., Giorgetta, M., Esch, M., Mauritsen, T., Crueger, T., Rast, S., Salzmann, M., Schmidt, H., Bader, J., Block, K., Brokopf, R., Fast, I., Kinne, S., Kornblueh, L., Lohmann, U., Pincus, R., Reichler, T., and Roeckner, E.: Atmospheric component of the MPI-M Earth system model: ECHAM6, Journal of Advances in Modeling Earth Systems, 5, 146–172, https://doi.org/10.1002/jame.20015, 2013.

Tarasov, L. and Peltier, W. R.: Greenland glacial history and local geodynamic consequences, Geophysical Journal International, 150, 198–229, https://doi.org/10.1046/j.1365-246x.2002.01702.x, 2002.

750 Tarasov, L., Dyke, A. S., Neal, R. M., and Peltier, W. R.: A data-calibrated distribution of deglacial chronologies for the North American ice complex from glaciological modeling, Earth and Planetary Science Letters, 315, 30–40, https://doi.org/10.1016/j.epsl.2011.09.010, 2012.

Tarasov, L., Hughes, A., Gyllencreutz, R., Lohne, O. S., Mangerud, J., and Svendsen, J.-I.: The global GLAC-1C deglaciation chronology, melwater pulse 1-a, and a question of missing ice, in: IGS Symposium on Contribution of Glaciers and Ice Sheets to Sea-Level Change, Chamonix-Mont-Blanc, France, 2014.

755 Tierney, J. E., deMenocal, P. B., and Zander, P. D.: A climatic context for the out-of-Africa migration, Geology, 45, 1023–1026, https://doi.org/10.1130/G39457.1, 2017a.

Tierney, J. E., Pausata, F. S. R., and deMenocal, P. B.: Rainfall regimes of the Green Sahara, Science Advances, 3, 1–9, https://doi.org/10.1126/sciadv.1601503, 2017b.

Tierney, J. E., Poulsen, C. J., Montañez, I. P., Bhattacharya, T., Feng, R., Ford, H. L., Hönisch, B., Inglis, G. N., Petersen, S. V., Sagoo,

760 N., Tabor, C. R., Thirumalai, K., Zhu, J., Burls, N. J., Foster, G. L., Goddéris, Y., Huber, B. T., Ivany, L. C., Turner, S. K., Lunt, D. J., McElwain, J. C., Mills, B. J. W., Otto-Bliesner, B. L., Ridgwell, A., and Zhang, Y. G.: Past climates inform our future, Science, 370, 1–9, https://doi.org/10.1126/science.aay3701, 2020a.

Tierney, J. E., Zhu, J., King, J., Malevich, S. B., Hakim, G. J., and Poulsen, C. J.: Glacial cooling and climate sensitivity revisited, Nature, 584, 569–573, https://doi.org/10.1038/s41586-020-2617-x, 2020b.

765 Tjallingii, R., Claussen, M., Stuut, J.-B. W., Fohlmeister, J., Jahn, A., Bickert, T., Lamy, F., and Röhl, U.: Coherent high- and low-latitude control of the northwest African hydrological balance, Nature Geoscience, 1, 670–675, https://doi.org/10.1038/ngeo289, 2008.

Tuenter, E., Weber, S. L., Hilgen, F. J., and Lourens, L. J.: The response of the African summer monsoon to remote and local forcing due to precession and obliquity, Global and Planetary Change, 36, 219–235, https://doi.org/10.1016/s0921-8181(02)00196-0, 2003.

Turney, C. S. M., Jones, R. T., McKay, N. P., van Sebille, E., Thomas, Z. A., Hillenbrand, C.-D., and Fogwill, C. J.: A global mean sea
770   surface temperature dataset for the Last Interglacial (129–116 ka) and contribution of thermal expansion to sea level change, Earth System Science Data, 12, 3341–3356, https://doi.org/10.5194/essd-12-3341-2020, 2020.

Wilkinson, R. D.: Bayesian calibration of expensive multivariate computer experiments, chap. Chapter 10, pp. 195–215, Wiley, https://doi.org/10.1002/9780470685853.ch10, 2010.

Yacoub, A. N., Sylvestre, F., Moussa, A., Hoelzmann, P., Alexandre, A., Dinies, M., Chalié, F., Vallet-Coulomb, C., Paillès, C., Darius,
775   F., Sonzogni, C., Couapel, M., Mazur, J.-C., and Kröpelin, S.: The African Holocene Humid Period in the Tibesti mountains (central Sahara, Chad): Climate reconstruction inferred from fossil diatoms and their oxygen isotope composition, Quaternary Science Reviews, 308, 1–17, https://doi.org/10.1016/j.quascirev.2023.108099, 2023.